



Deposited via The University of Leeds.

White Rose Research Online URL for this paper:

<https://eprints.whiterose.ac.uk/id/eprint/115597/>

Version: Accepted Version

---

**Article:**

Shivokhin, ME, Read, DJ, Kouloumasis, D et al. (2017) Understanding effect of constraint release environment on end-to-end vector relaxation of linear polymer chains. *Macromolecules*, 50 (11). pp. 4501-4523. ISSN: 0024-9297

<https://doi.org/10.1021/acs.macromol.6b01947>

---

© 2017 American Chemical Society. This document is the Accepted Manuscript version of a Published Work that appeared in final form in *Macromolecules*, copyright © American Chemical Society after peer review and technical editing by the publisher. To access the final edited and published work see <https://doi.org/10.1021/acs.macromol.6b01947>

**Reuse**

Items deposited in White Rose Research Online are protected by copyright, with all rights reserved unless indicated otherwise. They may be downloaded and/or printed for private study, or other acts as permitted by national copyright laws. The publisher or other rights holders may allow further reproduction and re-use of the full text version. This is indicated by the licence information on the White Rose Research Online record for the item.

**Takedown**

If you consider content in White Rose Research Online to be in breach of UK law, please notify us by emailing [eprints@whiterose.ac.uk](mailto:eprints@whiterose.ac.uk) including the URL of the record and the reason for the withdrawal request.

# UNDERSTANDING EFFECT OF CONSTRAINT RELEASE ENVIRONMENT ON END-TO-END VECTOR RELAXATION OF LINEAR POLYMER CHAINS.

Maksim E. Shivokhin<sup>1,2,3\*</sup>, Daniel J. Read<sup>4\*</sup>, Dimitris Kouloumasis<sup>5</sup>, Rok Kocen<sup>1</sup>, Flanco Zhuge<sup>1</sup>, Christian Bailly<sup>1</sup>, Nikos Hadjichristidis<sup>6</sup>, Alexei E. Likhtman<sup>7</sup>

<sup>1</sup>Bio- and Soft Matter division (BSMA), Institute of Condensed Matter and Nanosciences (IMCN), Université Catholique de Louvain (UCL), Place Croix de Sud 1, 1348 Louvain-la-Neuve, Belgium

<sup>2</sup>Center for molecular study of condensed soft matter and Department of Chemical and Biological Engineering, Illinois Institute of Technology, 3440 South Dearborn Street, Chicago, Illinois 60616, USA

<sup>3</sup>Current affiliation: ExxonMobil Chemical Company, Baytown Technology and Engineering Complex, 5200 Bayway Drive, Baytown, Texas 77520, USA

<sup>4</sup>School of Mathematics, University of Leeds, Leeds LS2 9JT, U.K

<sup>5</sup>Laboratory of Industrial Chemistry, Department of Chemistry, University of Athens, Panepistimiopolis Zografou, 157 71 Athens, Greece

<sup>6</sup>Physical Sciences and Engineering Division, KAUST Catalysis Center (KCC), Polymer Synthesis Laboratory, King Abdullah University of Science and Technology (KAUST), Thuwal 23955-6900, Kingdom of Saudi Arabia

<sup>7</sup>School of Mathematical and Physical Sciences, University of Reading, Reading RG6 6AX, U.K.

\* Authors to whom correspondence should be addressed.

D.J.R. : [d.j.read@leeds.ac.uk](mailto:d.j.read@leeds.ac.uk)

M.E.S. : [maksim.e.shivokhin@exxonmobil.com](mailto:maksim.e.shivokhin@exxonmobil.com)

*We dedicate this article to the co-author of this work, our colleague and dear friend Alexei E. Likhtman.*

## Abstract

In this study we propose and verify methods based on the slip-spring (SSp) model (*Likhtman, 2005*) for predicting the effect of any monodisperse, binary or ternary environment of topological constraints on the relaxation of the end-to-end vector of a linear probe chain. For this purpose we first validate the ability of the model to consistently predict both the viscoelastic

and dielectric response of monodisperse and binary mixtures of type-A polymers, based on published experimental data. We also report the synthesis of new binary and ternary Polybutadiene systems, the measurement of their linear viscoelastic response, and the prediction of these data by the SSp model. We next clarify the relaxation mechanisms of probe chains in these constraint release (CR) environments by analyzing a set of “toy” SSp models with simplified constraint release rates, by examining fluctuations of the end-to-end vector. In our analysis, the longest relaxation time of the probe chain is determined by a competition between the longest relaxation times of the effective CR motions of the fat and thin tubes, and the motion of the chain itself in the thin tube. This picture is tested by the analysis of four model systems designed to separate and estimate every single contribution involved in the relaxation of the probe’s end-to-end vector in polydisperse systems. We follow the CR picture of (*Viovy et al., 1991*) and refine the effective chain friction in the thin and fat tubes based on (*Read et al., 2012*). The derived analytical equations form a basis for generalizing the proposed methodology to polydisperse mixtures of linear and branched polymers. The consistency between the the SSp model and tube model predictions is a strong indicator of the compatibility between these two distinct mesoscopic frameworks.

### List of variables and functions

In order to help the reader we summarize and describe all variables and functions used in the text in the table below.

Variable or function	Description
<b>Relaxation times</b>	
$\tau_{d,s}$	Longest relaxation time of the short chains in section 3 obtained by simulations with no constraint release
$\tau_{d,p}$	Longest relaxation time of the probe chains in section 3 obtained by simulations with no constraint release
$\tau_d$	Longest relaxation time of the probe chains with no constraint release predicted by eq.1

$f(Z)$	Correction to the reptation time due to the effect of contour length fluctuation
$\tau_{CR}$	Lifetime of the slip-links in case when all of them are blinking with same frequency.
$\tau_{CR,TT}$	Lifetime of slip-links blinking with higher frequency in the case when there are at least two distinct frequencies.
$\tau_{CR,FT}$	Lifetime of slip-links blinking with lower frequency in the case when there are at least two distinct frequencies.
$\tau_{CRR,TT}$	The longest relaxation time due to the CR Rouse motion of the thin tube
$\tau_{TT}$	Relaxation time of the probe chain due to the effective CR motion of the thin tube
$\tau_{FT}$	Relaxation time of the probe chain due to the Rouse CR motion of the fat tube
$\tau_p^{(2)}$	Longest relaxation time of the probe chain having all slip-links blinking with the same frequency
$\tau_p^{(3)}$	Longest relaxation time of the probe chain having some slip-links blinking with single frequency while others are permanent
$\tau_p^{(4)}$	Longest relaxation time of the probe chain having slip-links blinking with two distinct frequencies.

<b>Friction coefficients</b>	
$\zeta_{CR,TT}$	Friction due to CR hopping of the thin tube in 3D space (section 6.2) or along fat tube (sections 6.3, 6.4)

$\zeta_{CR,FT}$	Friction due to CR hopping of the fat tube in 3D space
$\zeta_{TT}$	Total friction of the thin tube motion in 3D space
$\zeta'_{TT}$	Total friction of the thin tube constrained by a fraction of slip-links with infinite constraint release time.
$\zeta_{FT}$	Total friction of the fat tube motion in 3D space
$\zeta_0^{cm}$	Center of mass friction of the probe chain.
$\zeta_{0,SL}$	Friction contribution to longitudinal chain motion due to hopping slip-links.
$\zeta_{eff}$	Effective friction of the chain in its projected motion along the fat tube contour
$\zeta_+$	Additional friction contribution due to the blinking nature of the topological constraints in the case when there are at least two distinct CR rates.
$\zeta_p^{(3)}$	Total friction coefficient of the probe chain with some slip-links blinking with constant frequency and others with infinite constraint release time.
$\zeta_p^{(4)}$	Total friction coefficient of the probe chain with slip-links blinking with two frequencies $\tau_{CR,TT}$ and $\tau_{CR,FT}$ .
$\zeta^{MSD}$	Obtained from simulated MSD of chain's center of mass total friction coefficient of the probe chain constrained by slip-links blinking with the same frequency and moving in 3D space.

## 1. Introduction.

The basic tube model initially proposed by Doi, Edwards and de Gennes<sup>4,5,8</sup> describes the dynamics of a probe chain in a fixed environment of topological constraints. It is a “single body” description, with the meaning that such an expression carries in physics and mechanics. On the other hand, the real situation is clearly a simultaneous multibody relaxation, with complex feedback effects. Not surprisingly, a correct description of the effect of multi-chain environment on the probe chain relaxation still remains a challenging issue.

The first models implementing the effects of constraint release (CR) considered the tube as a Rouse chain with segments having the size of the tube diameter.<sup>3,12</sup> Mobility of the segments was considered to be inversely proportional to the lifetimes of the entanglements. We refer to these models as tube rearrangement models. An alternative picture for modeling the effect of constraint release (CR) on stress relaxation was introduced by Marrucci<sup>17</sup>. Marrucci suggested the previously relaxed fraction of the melt should be considered as an effective solvent for still oriented chain segments. This so-called dynamic tube dilation (DTD) theory pictures an effective tube diameter continuously widening in the course of stress relaxation and thereby facilitating chain motion. Doi and co-workers in ref. <sup>9</sup> proposed to combine both CR pictures and defined the effective tube diameter as a crossover between mean squared displacement of the free chain and motion of the tube described by Rouse dynamics. Finally, Viovy and co-workers<sup>28</sup> further extended the original tube rearrangement picture for the case of binary linear melts. They proposed that CR motion of the tube should be effectively separated in two regimes: (i) CR Rouse motion, which is only relevant in the diffusion scale limited by the fat tube diameter and (ii) further relaxation of the tube governed by CR reptation of a thin tube along the fat tube contour.

Regardless of the CR picture used, most authors have adopted the assumption of independent contributions from the tube and chain motions. Thus for computing the overall stress relaxation function, the two contributions are then combined by a multiplicative mixing law.

The ability to experimentally separate the relaxation of a probe chain in its tube from the relaxation of the environment is an important issue since it can help discriminate between CR

models. Whereas linear rheology measurements conflate all relaxation mechanisms (reptation, fluctuations and constraint release) in a single response, other techniques can distinguish between different effects. Among those, dielectric spectroscopy measures the relaxation of dielectric permittivity  $\epsilon(t)$  usually from the frequency response through Fourier analysis. This technique is attractive as a complement to rheological measurements and is widely used to study relaxation dynamics of polymers. Its limitation comes from the requirement that non canceling electrical dipoles have to be present along the chain. For the so-called “type-A” polymers having dipoles parallel to the chain backbone<sup>25</sup> relaxation of an induced polarization of the chain is equivalent to the fluctuation of its end-to-end vector. As an alternative to this method C.-Y. Liu and co-workers<sup>16</sup> proposed an experimental probe rheology method for studying relaxation contributions due to the tube motion. In binary melts they suppressed the relaxation contribution from the environment by diluting short probe chain in an excess of much longer matrix chains. By assuming that relaxation spectra of the probe and matrix are uncoupled, they subtracted the relaxation function of the probe and considered it as being unaffected by CR. Despite its obvious theoretical value, application of this method is limited in terms of the probe concentration. The concentration of the probe should be very low in order to avoid CR effect from entanglements with chains of the same molecular weight. Moreover, the matrix should not be affected by dynamics of the probe. This can be tested by comparing the terminal relaxation time of the matrix with and without the probe. On the other hand the low concentration of the probe is automatically reflected in the low intensity of the subtracted signal.

H. Watanabe and co-workers in various publications have extensively used a combination of linear rheology and dielectric spectroscopy on Polyisoprene (PI) (typical type-A polymer) for understanding the effect of the environment on the viscoelastic relaxation of the polymer. As opposed to viscoelastic relaxation, no dielectric relaxation of the chain is activated by the motion of its environment, except for a contribution from chain fluctuations at the edge of the dilated tube.<sup>29</sup> Hence, the tube survival fraction,  $\phi'(t)$ , can be directly extracted from the dielectric relaxation function  $\Phi(t)$ . The authors find that viscoelastic relaxation is linked to dielectric relaxation in a straightforward way for monodisperse linear PI:  $\mu(t) = G(t)/G_N^0 = \phi'(t)^{1+d}$ , where  $G_N^0$  - plateau modulus and  $d$  ( $=1..1.3$ ) is the dilation exponent. This confirms a direct relationship between two relaxation functions.

The effect of environment represented by constraint release (CR) on the relaxation of the end-to-end vector in monodisperse star and linear polymers and binary blends of linear chains has been addressed by many authors but a clear picture has yet to emerge. The most recent publications include:

- In ref.<sup>19</sup> authors applied a discrete slip-link model (DSM) in order to predict experimental data of the viscoelastic and dielectric relaxation functions in monodisperse melts of linear and star polymers and binary mixtures of short and long linear chains. In agreement with ref.<sup>11</sup> they concluded that the end-to-end vector autocorrelation function of monodisperse *linear* chains is not affected by their CR dynamics. In contrast, relaxation of the end-to-end vector of monodisperse *star* polymers is drastically influenced by constraint dynamics.
- Matsumiya et al.<sup>18</sup> investigated the effect of CR on the dielectric relaxation of short PI chains with number of entanglements ranging between 4 and 36, diluted in an excess of much longer chains. They concluded that the end-to-end vector relaxation time of all the diluted short chains is significantly delayed by comparison with bulk probe systems but is faster than expected from utilizing full dynamic tube dilation theory.

The main objective of this study is to understand the effect of various molecular constraint dynamics on relaxation of the end-to-end vector of long linear probe chains. In contrast with Matsumiya et al.<sup>18</sup>, we will focus primarily on situations in which a probe chain is placed in an environment in which a fraction of the constraint release events are at a rate faster than the reptation time of the probe chain (Matsumiya et al. focus on slower CR environments). We approach this problem by utilizing the Likhtman's slip-spring (SSp) model.<sup>13,21</sup> This model naturally includes stress relaxation mechanisms such as reptation, contour length fluctuations (CLF) and constraint release (CR), which are also implemented in the tube-based models. The advantage of this single-chain model is that it also allows for independent control of each of the stress relaxation mechanisms. By using this convenient feature we progressively increase the complexity of the constraint release environment for the probe chain by considering *four model systems* which are specifically chosen in order to highlight the various CR contributions to relaxation of the end-to-end vector. We successively create experimental systems which

approximate these idealized model systems, and analyze SSp simulations of the idealized models.

We first validate the SSp model by simultaneous comparison with experimental rheo-dielectric relaxation data from the literature and with linear rheology data for specially prepared binary and ternary mixtures of linear chains with well separated molecular weights. Next, from simulations of the SSp model, we extract the longest relaxation times of the end-to-end vector of the probe chain in different constraint release environments and analyze the results in the frame of the tube model. To succeed in this step we rely on methodology proposed by Read<sup>22</sup> and later utilized by Shivokhin et al.<sup>24</sup> for computing the total friction coefficient for motion along the fat tube in star/linear blends. In this work we aim to further extend this approach and compute longest end-to-end vector relaxation time of the probe chain in similar and even more complex CR environments.

It should be emphasized from the outset that we are seeking in this work to relate the results obtained from the SSp model, to the corresponding description in the framework of the tube model. These two modelling frameworks are not identical, and it is not *a priori* obvious that ideas based on the tube model (e.g. for motion along a “fat tube”) will apply to SSp simulations. So, this work constitutes an interesting test of the correspondence between these two mesoscopic approaches to describing the motion of entangled chains.

As this study is fundamentally an illustration of a methodology that can be extended to systems with variable CR complexity, we allow some simplifications that do not influence the final objective but significantly facilitate derivation of the final equations. In our analytical equations we do not account for the distribution of CR times in every component of the mixture. Instead, for every component of the blend, we only consider the largest possible constraint release time represented by its reptation time.

This paper is arranged as follows: in the methodology section we introduce the four main model systems characterized by dominant constraint release contributions. In the experimental section we describe details of the synthesis and molecular structure of the materials. We also provide details of the small angle oscillatory shear measurements and data processing. The theoretical section describes the necessary details of the SSp model. In the results and discussion section, we validate the SSp model by comparison with the dielectric and linear rheology data. Next, individually for every model system we propose straightforward analytical equations predicting

the corresponding longest relaxation times and validate them by stochastic simulations of the accordingly modified SSp models. In the conclusion, we summarize the key results of this study and highlight possible perspectives.

## 2. Methodology

For analyzing the effect of a binary CR environment formed by short and long chains, we adopt the picture of thin and fat tubes constraining lateral motion of the chain. The thin tube is formed by entanglements of a given probe chain with all chains, whereas the fat tube includes only entanglements with longer life time.

We propose a picture where the longest relaxation time of the probe chain end-to-end vector is determined by a competition between the longest relaxation times of the effective CR motions of the fat and thin tubes as well as the motion of the chain itself in the thin tube (see Figure 1). In order to test this picture we define *4 model systems* which are specifically selected in order to separate and estimate every single contribution involved in the relaxation of the probe's end-to-end vector in the binary blend system (see Figure 2).

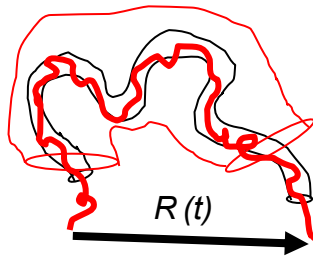


**Figure 1:** Schematic representation of a probe chain in a binary CR environment (system #4). Topological constraints respectively due to the mixed entanglements with short and probe chains vs. entanglements with probe chains only are illustrated by the black thin tube, and the red fat tube. The end-to-end vector of the probe chain is shown by the solid black arrow.

### Probe chain in fixed environment:

In the 1<sup>st</sup> system we dilute probe chains in the sea of very long chains, which are not relaxing at the time scale of the observations (below referred to as “gel”). In this system probe chains are not entangled with other probe chains, but only with the “gel”. Hence, CR is essentially turned off for the probe chains. The only possible relaxation mechanism is by reptation motion

of the chain in the thin tube, with contour length fluctuations. This mechanism is of course also present in all other systems.

**Probe chain inside single moving tube:**

In the system #2 all entanglements of the chain are blinking with the same finite frequency. Therefore constraint release dynamics is competing with chain reptation along the thin tube.

**Probe chain in thin tube moving inside fixed fat tube:**

The 3<sup>rd</sup> system is the mixture between first two systems, where a fraction  $1 - f$  of entanglements of the probe chain are created by the short chains and the rest are created by the gel. By doing this, and assuming that long chains of the gel are effectively immobile at the timescale of relaxation of the probe chains, we get a controlled amount of CR. This mobile fraction of entanglements leads to CR motion of the thin tube, itself partially constrained by the fat tube (entanglements with gel chains).

**Probe chain in moving thin and fat tubes:**

In the 4<sup>th</sup> system the probe chain is entangled with short and long chains having two distinct CR rates. A fraction  $f$  of the probe chain's entanglements is with longer chains. The complementary fraction  $1 - f$  with short chains is the same for the 3<sup>rd</sup> and 4<sup>th</sup> systems.

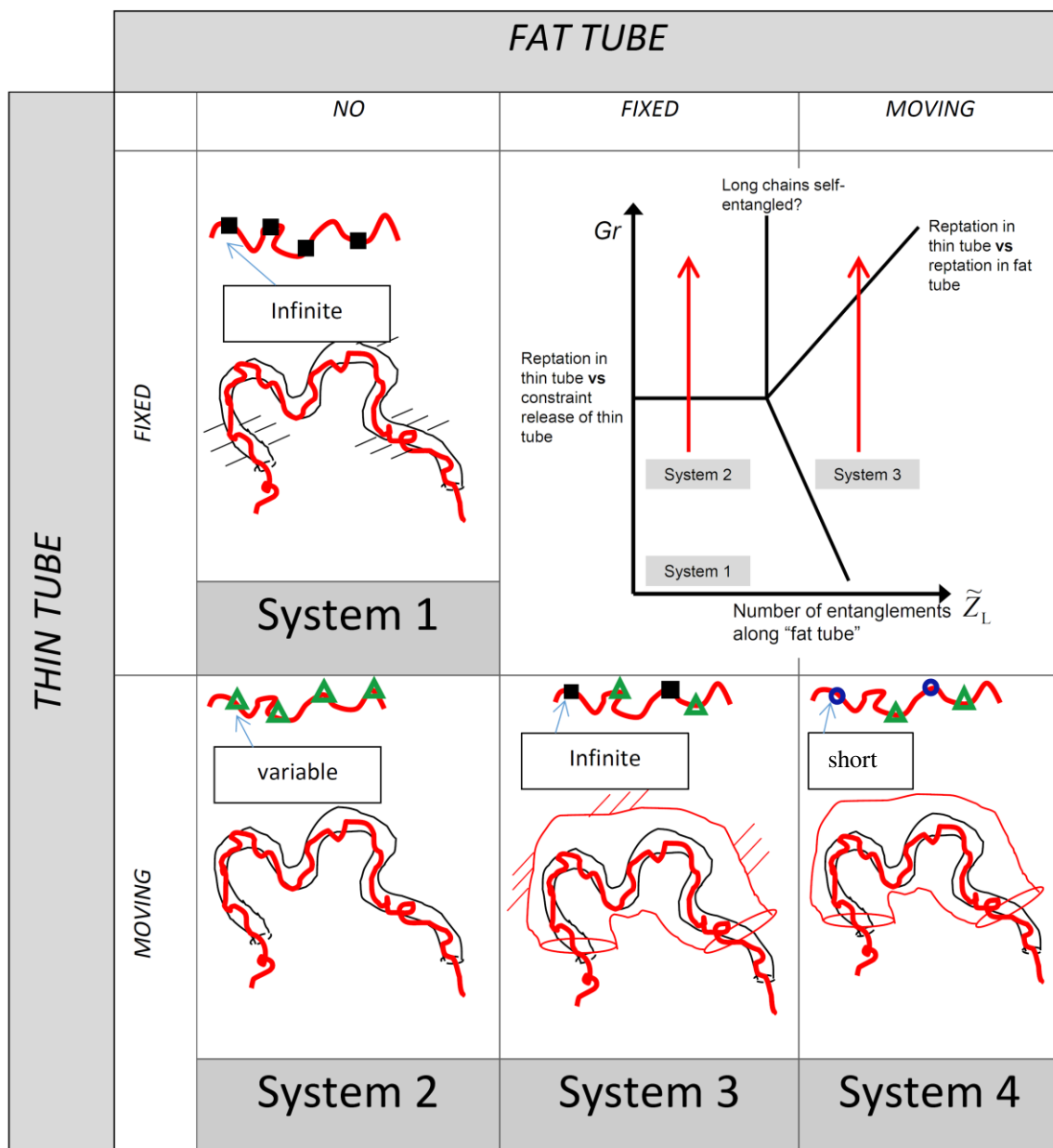


Figure 2: The four model systems of the probe chain in the “idealized” single and binary CR environments schematically shown in tube and slip-link model representation. *System 1*: probe chain in a “gel” (infinite CR time); *System 2*: probe chain with varying CR time. *System 3*: probe chain with varying and infinite CR times. *System 4*: probe chain with short and varying CR times. At the upper part of all pictures a probe chain is shown by the red solid line, slip-links with “infinite” CR time are shown by filled black squares. Empty blue circles represent slip-links with short CR time and empty green triangles-varying CR time. At the lower part of all pictures the respective tube model representation is shown. The thin tube is illustrated by solid black lines; fat tube is shown by solid red lines. Inset: (top right) locating systems 1 – 3 on a “Viovy diagram”. Arrows indicate increasing rates of constraint release.

The first three systems may be located on the “Viovy diagram” for binary blend rheology as shown in the inset of Figure 2.<sup>22</sup> On the horizontal axis is the number of entanglements in the

fat tube, and so to the left of the diagram no fat tube entanglements are important and there is a single constraint release rate. The vertical axis, the “Graessley parameter” is a measure of the rate of constraint release. Hence system 1 corresponds to just one (thin) tube and no constraint release – the bottom left of the Viovy diagram. System 2 corresponds to one thin tube and varying CR rate, which is equivalent to traveling up the left hand side of the diagram. We may anticipate that one transition to be encountered involves a competition between reptation along the thin tube and CR of the thin tube. System 3 corresponds to a situation where fat tube entanglements are important, and we may anticipate at the least a competition between reptation along the thin tube, and motion along the fat tube mediated by constraint release.

In this study, we use the single-chain SSp model for simulations of equilibrium polymer dynamics.<sup>13</sup> This model allows the estimation of the stress relaxation and end-to-end vector autocorrelation function of every blend component individually without relying on any subtraction procedure.

First, we validate the model by simultaneous comparison with published data of the stress relaxation and dielectric relaxation in nearly monodisperse and binary mixtures of linear polymers. Next, we use our own rheology data in order to estimate the end-to-end vector autocorrelation function of the probe chain in different model systems by means of the SSp model. Since simulations of the end-to-end vector autocorrelation function can be conducted for any type of polymer we are not restricted to type-A polymers traditionally used in the dielectric spectroscopy experiments.

In order to obtain the longest relaxation time of the end-to-end vector in every system we fit the respective end-to-end vector autocorrelation function to a set of Maxwell modes using RepTate software and extract the relaxation time of the longest mode.<sup>20</sup>

### **3. Experimental section**

#### **3.1. Materials**

The synthesis details for the linear Polybutadiene (PBd) samples with  $M_w \sim 6.9 \text{ kg/mol}$  (PDI=1.08,  $T_g = -97^\circ\text{C}$ ) and  $M_w \sim 50 \text{ kg/mol}$  (PDI=1.06,  $T_g = -95^\circ\text{C}$ ) with 90.3% and 90.6% of 1,4 addition, respectively, have been reported in ref.<sup>24</sup>

Linear PBd with  $M_w \sim 305\text{k}$  (PDI=1.08,  $T_g = -96^\circ\text{C}$ ) with 93.2% of 1,4 addition was purchased from Polymer Source, Inc.

The glass transition temperatures are measured using Mettler Toledo DSC 821e at heating rate  $10^\circ\text{C}/\text{min}$ .

The 1,4 addition levels of the samples were measured by  $^1\text{H-NMR}$ , via spectra recorded on 300 MHz Bruker spectrometer at  $25^\circ\text{C}$ .

All the experimental details including the NMR spectra, SEC chromatograms, and DSC thermographs are provided in the supporting information.

Throughout the study, samples with molecular weights 6.9k, 50k and 305k will be referred to as short, probe and “gel” chains, with molecular weights  $M_{w,s}$ ,  $M_{w,p}$  and  $M_{w,G}$ , and their longest relaxation times  $\tau_{d,s}$ ,  $\tau_{d,p}$ ,  $\tau_{d,G}$ , respectively. In the second half of this paper (section 6 and Appendices) we analyze the effect of the “simplified” CR environment imposed on the dynamics of the probe chain by the short chains, “gel”, and other probe chains.

All blends analyzed in this study are fully miscible. They are prepared by mixing in an excess of toluene. After complete dissolution of the polymer by continuous stirring during 1-2 days the solvent is evaporated in a vacuum oven for at least 7-10 days until the sample has less than 0.1% of solvent left (as measured by weight loss).

### **3.2. Measurements**

In this section we present results of experimental SAOS measurements for all model systems introduced in the methodology section. All measurements are done using an ARES (TA Instruments) rheometer equipped with a plate-plate fixture of 8 mm diameter. The linear range of sample deformations was confirmed by conducting strain-sweep measurements.

After conducting frequency-sweep measurements at 25, 0, -25, -50 and  $-70^\circ\text{C}$  under nitrogen atmosphere, we apply the time-temperature superposition principle (TTS) for constructing master curves covering a much broader range of frequencies as compared to the individual master curve segments measured at constant temperature. Unlike many publications which used adjustable shift factors for every measurement, we determine shift factors using the WLF

equation  $\log_{10}a_T = -C_1(T-T_{ref})/(C_2+T-T_{ref})$ , where parameters  $C_1=3.63$ ,  $C_2=167.11$  K at  $T_{ref}=25^\circ\text{C}$  are kept the same for all samples.

By introducing iso-free-volume correction to the horizontal shift-factors we account for differences in components'  $T_g$  due to their different molecular weights:  $\log_{10}a_T = -C_1(T-T_{ref}+C_{Tg}/M_w)/(C_2+T-T_{ref}+C_{Tg}/M_w)$ , where  $C_{Tg}/M_w = (T_g^{inf} - T_g)$  and  $C_{Tg} = 13$  is an empirical Flory–Fox parameter that is related to the free volume for a given polymer chemistry.<sup>10</sup>

We also note, that while short and probe chains were made in the same lab and the same batch as samples reported in ref.<sup>24</sup>, the “gel” chains were obtained from another source and have a slightly different microstructure as demonstrated by the NMR data. As a result of this slight difference the correspondent glass transition temperature of this sample, as measured by DSC, is slightly lower than could be expected for its molecular weight. We disregarded these differences in the TTS procedure used for the data presented in Figures 7-8.

Material density correction due to the temperature change is taken into account by introducing vertical shift factors as  $G(T_{ref})=G(T)/b_T$ , where  $b_T = \rho(T)T/\rho(T_{ref})T_{ref} = (\rho(T_{ref})+T.C_3.10^{-3})(T+273.15)/(\rho(T_{ref})+T_{ref}.C_3.10^{-3})(T_{ref}+273.15)$ , where  $T$  is in  $^\circ\text{C}$ ,  $\rho(T_{ref})=930$   $\text{kg.m}^{-3}$ , and  $C_3=0.69$   $\text{kg.m}^{-3}/^\circ\text{C}$ . The obtained results represented by frequency sweep data of storage and loss moduli are compared with predictions of the SSp model in Figures 7-9.

#### 4. The SSp model.

All numerical simulations in this study are conducted using Likhtman's stochastic single chain SSp model.<sup>13</sup> This model is based on Rouse chains comprising  $N$  beads connected by  $N-1$  springs. The effect of entanglements is implemented by slip-links randomly distributed along the chain. Every slip-link is connected by a virtual spring with parabolic potential to an anchoring point. The positions of the anchoring points are distributed in a way to preserve unperturbed Gaussian statistics of the chain conformations at all length scales.

Successful applications of this model for predicting stress relaxation in low polydispersity linear and binary mixtures of star and linear entangled polymer melts were reported in refs.<sup>13,24</sup> Besides, in ref.<sup>13</sup> the model has demonstrated quantitative prediction capability of polymer

dynamics when simultaneously confronted with experimental data by three different techniques: neutron spin-echo (NSE), linear rheology and molecular diffusion.

Most implementation details and description of the model parameters can be found elsewhere.<sup>13,21</sup> In these earliest versions of the SSp model, the location of the slip-link was allowed to slide continuously along the bond vector between adjacent beads. However, more recent versions of the algorithm<sup>14,24</sup> have constrained the “slip-links” so that they are always attached to beads. Slip-link hopping between beads is permitted through Metropolis Monte Carlo moves. Our simulations are based on this later methodology. We analyze in detail the effect of this choice in section 6 below, finding that it results in an effective contribution to chain sliding friction from the slip-links.

In this study we also utilize a number of simplified “toy models” based on this SSp implementation in order to separate relaxation contributions. In particular, we can deactivate reptation and CLF mechanisms by prohibiting slip-links from sliding over the chain ends. We can also assign precise single engagement/disengagement frequencies for slip-links (as opposed to self-consistently distributing constraint release by coupling slip-links from different chains). In particular, in order to realize the different systems indicated in Figure 2 we are required to maintain up to two different populations of slip-springs with two different assigned CR rates (slow and fast). In our simulations, this is achieved by separately controlling the reptation/CLF and constraint release dynamics. For the CR dynamics, each slip-spring from a given population (e.g. the “slow” slip-springs) is assigned a lifetime randomly chosen from an exponential distribution with mean equal to the CR time of that population. When a slip-spring exceeds its lifetime, it is removed from the simulation, and a new slip-spring from the same population (e.g. “slow”) is added to a randomly selected point on a randomly selected chain, and given a new randomly chosen lifetime. On the other hand, if a slip-spring from a given population (e.g. a “slow” slip-spring) is removed from a chain end by reptation and CLF, then another slip-spring of the same type (e.g. “slow”) is added to the *end* of a randomly selected chain, and assigned a random lifetime. This latter rule ensures that creation and destruction of slip-springs from chain ends do not produce CR events in the middle of chains. The simulation rules, as presented above, are in the spirit of the standard entanglement-pairing CR algorithm described in ref.<sup>13</sup> but decouple the CR dynamics from the reptation dynamics, whilst maintaining a constant number of fast and slow slip-springs in the simulation. An alternative but valid approach, not used in our simulations, would be (for constraint release) to randomly add and

delete slip-springs from the middle of chains using a detailed balance criterion with rates chosen to ensure the correct slip-spring lifetimes, and similarly (for reptation/CLF) to add and delete slip-springs from chain ends using a different detailed balance criterion. This alternative approach would maintain the *average* number of fast and slow slip-links, while allowing both to fluctuate.

Thus, by assigning infinite lifetime to the slip-links we can completely “shut down” the relaxation contribution from CR. In this way, we are able to separate, control and analyze relaxation contributions due to sliding and CR dynamics of the chain. We note that by introducing controlled CR rates we do not attempt to impose self-consistency of the CR events, e.g. by selecting CR rates consistent with the reptation time of the chains. However, this is not important for the purpose of the second half of this paper which is focused on understanding the effect made by various “artificial” CR environments on the dynamics of dilute probe chains.

On the other hand, for simulations of the stress relaxation for the purpose of comparing it with experimental data for monodisperse, binary and ternary mixtures in section 5 we use the standard entanglement-pairing CR algorithm described in ref.<sup>13</sup> which automatically gives a self-consistent distribution of CR rates. The number of chains corresponding to every blend component in simulations is computed in accordance with its respective weight fraction. We first fit the elementary time,  $\tau_0$ , and unit mass parameter,  $M_0$ , represented by one bead in SSp model for all monodisperse components. Next, all binary and ternary mixtures are predicted without additional parameter fitting. The slight discrepancy between the values of  $M_0$  obtained for different blend components (see Table 1) is in the range of typical SEC measurements experimental error.

The SSp simulations results are presented in dimensionless units, with thermal energy  $k_B T=1$ , statistical segment  $b=1$  and friction coefficient of one segment  $\zeta_0=1$ . Regardless of molecular topology and molecular weight we use  $N_{e,ss}=4$  as average number of beads between two slip-links,  $N_s=0.5$  as virtual spring strength, and time step  $dt=0.05$ . For the results in section 5, a discrete slip-link jump of size 1 is attempted on average once per bead at every time step in a Metropolis Monte Carlo simulation as described in ref.<sup>14</sup> In section 6, we increase this to 10 attempts per time-step. Finally, in this work we use a variant of the SSp model which imposes the condition that the monomer distance between neighboring slip-links must be larger than 1 thereby preventing two slip-links from overlapping or occupying neighboring beads. This

repulsive interaction has weak effects on both statics (making the slip-spring distribution more uniform along the chain) and dynamics (e.g. on rates of slip-spring motion, and of creation and destruction rates at chain ends).

From these simulations we extract stress relaxation functions and end-to-end vector autocorrelation functions for every component.<sup>14,21</sup> For computing stress relaxation we take into account non-negligible cross-correlation contributions from the virtual springs along the chain.<sup>21</sup> For simulating blends both auto- and cross-correlation terms of stress relaxation are weighed in accordance with weight fractions of the respective blend component. The cross-correlation term is not considered for computing relaxation of end-to-end vector.

For mapping the time and stress of the model to those of the experimental data, we multiply them by  $\tau_0$  and  $G_0$  or  $\varepsilon_0$ , respectively (see Table 1).

**Table 1: Fitted values of the SSp model parameters.**

	$T_{ref}, ^\circ C$	$M_0, \text{kg/mol}$	$\tau_0, \mu\text{s}$	$G_0, \text{MPa}$
PI	40	1	6.83	2.85
PI	25	1	12.1	2.71
PBd	25	0.38	0.45	7.0

The obtained parameters for PBd are consistent with those of previously analyzed star and linear polymers.<sup>6</sup>

It should be noted that the stress of the model is calculated in units of  $G_0 = \rho RT/M_0$  with  $\rho$ ,  $R$  and  $T$  being the polymer density, universal gas constant and absolute temperature, respectively. By using  $\rho(\text{PBd, PI}) = 930$  and  $913 \text{ kg/m}^3$ ,  $T(\text{PI}) = 313 \text{ K}$ ,  $T(\text{PBd}) = 298 \text{ K}$ ,  $R = 8.31 \text{ m}^3 \cdot \text{Pa} \cdot \text{K}^{-1} \cdot \text{mol}^{-1}$  and by substituting the fitted values of  $M_0$  we can compute  $G_0(\text{PBd}) = 6.06 \text{ MPa}$  and  $G_0(\text{PI}) = 2.37 \text{ MPa}$ . The obtained values are slightly different from the fitted  $G_0$ : 13 and 17% for PBd and PI, respectively. The value of  $G_0$  of PI at  $T_{ref} = 25^\circ \text{C}$  is computed in accordance with the temperature change assuming its fitted value at  $40^\circ \text{C}$  as a reference. This level of discrepancies is consistent with data variations reported in different papers. The model stress  $G_0$  should not be confused with the plateau modulus  $G_N^0$ .

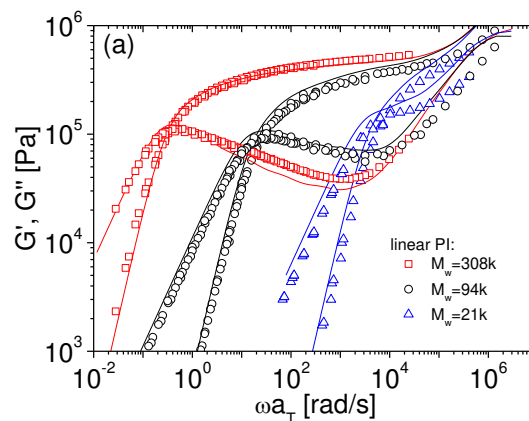
## 5. Comparison between the SSp model simulations and experimental data on binary and ternary blends

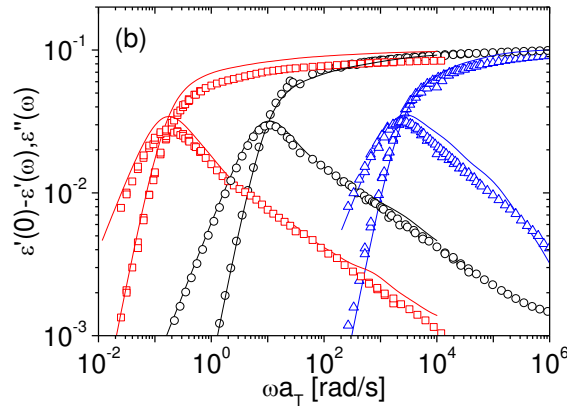
### 5.1. Comparison with literature data.

Dielectric relaxation of type-A polymers reveals the end-to-end vector autocorrelation function. According to our knowledge, the simulation results of the SSp model have never been confronted in published literature with experimental dielectric relaxation data. In this section we validate the SSp model by comparison with published data of Watanabe et al. in references<sup>30</sup> on dielectric and viscoelastic relaxation of the same PI melts at the same reference temperature.

The model parameters  $M_0$ ,  $\tau_0$  and  $G_0$  are calibrated by fitting small angle oscillatory shear (SAOS) data for monodisperse linear chains of  $M_w=21$  kg/mol, 94 kg/mol and 308 kg/mol. The stress relaxation and end-to-end vector autocorrelation function are predicted from the same simulations. Therefore, after we have fitted material parameters on SAOS data for both monodisperse components, the stress and dielectric relaxations in all blend compositions are predicted without additional adjustment of the parameters. On the other hand, in section 6, where we compare simulation results with predictions of the equivalent tube model, we need to introduce additional parameters which will be discussed later in the text.

In Figure 3 we show a comparison between experimental (rheological and dielectric) data and the SSp model predictions with the same set of parameters.

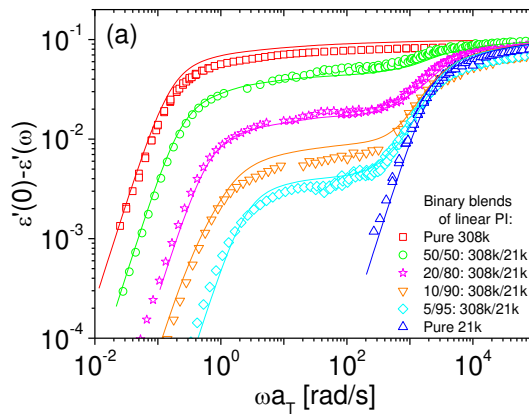




**Figure 3:** Comparison of simulation results with experimental dynamic rheological (a)  $G'(\omega)$ ,  $G''(\omega)$ , and (b) dielectric  $\varepsilon'(0)-\varepsilon'(\omega)$ ,  $\varepsilon''(\omega)$  data of monodisperse linear PI with  $M_w=21$  kg/mol, 94 kg/mol and 308 kg/mol. Symbols represent experimental data and lines indicate the SSp predictions. All simulations are made with material parameters  $M_0=1$  kg/mol,  $G_0=2.85$  MPa;  $\varepsilon_0=0.1$ ;  $\tau_0=6.83$   $\mu$ s. The experimental data are measured at  $T_{ref}=40^\circ\text{C}$ . Color code in (a) and (b) is the same.

Besides some small discrepancy (in the range of 15%) observed between the experiments and simulations in Figure 3 all simulation results demonstrate quantitative prediction of both rheological and dielectric data using the same values of the parameters.

Next, in Figure 4 and Figure 5 we analyze the SSp prediction for binary mixtures of linear PI. For this purpose, we superimpose predictions of the SSp model with the experimental data of complex dielectric permittivity and complex viscoelastic relaxation modulus of different ratios 0/100, 5/95, 10/90, 20/80, 50/50 and 100/0 of 308k/21k.



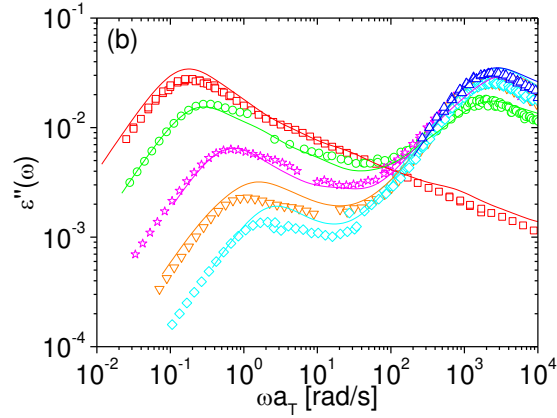


Figure 4: Comparison between simulation results and experimental (a) decrease of dynamics dielectric constant,  $\varepsilon'(0)-\varepsilon'(\omega)$ , and (b) dielectric loss,  $\varepsilon''(\omega)$ , of monodisperse and binary mixtures of linear PI with  $M_w=21$  kg/mol and 308 kg/mol. Symbols represent experimental data and lines indicate SSp predictions. All simulations are obtained with material parameters  $M_0=1$  kg/mol,  $\varepsilon_0=0.1$ ;  $\tau_0=6.83$   $\mu$ s. The experimental data is measured at  $T_{ref}=40^\circ$ C. Color code in (a) and (b) is the same.

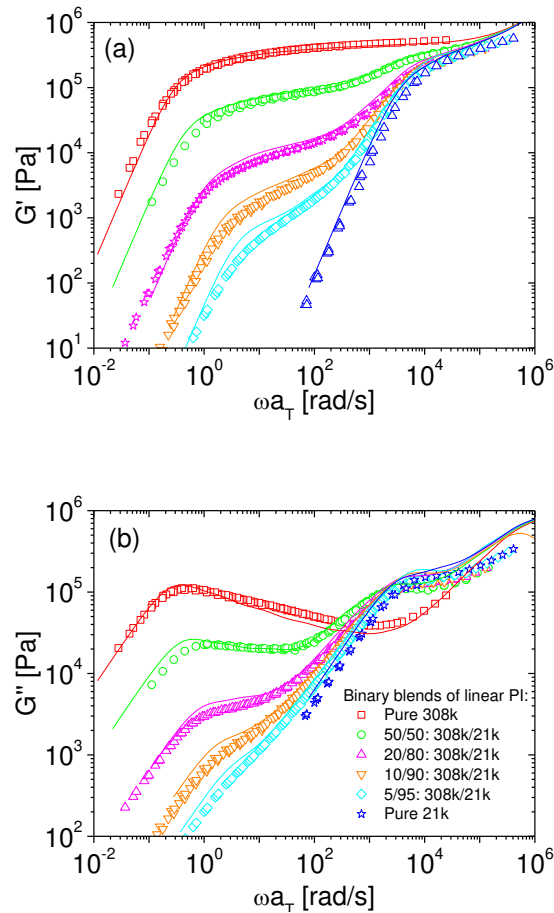


Figure 5: Comparison between simulation results and experimental (a) dynamic storage,  $G'(\omega)$ , and (b) loss,  $G''(\omega)$ , moduli of monodisperse and binary mixtures of linear PI with  $M_w=21$  kg/mol and 308 kg/mol. Symbols represent experimental data and lines indicate SSp predictions. All simulations are obtained with

material parameters  $M_0=1$  kg/mol,  $\tau_0=6.83$   $\mu$ s,  $G_0=2.71$ MPa. The experimental data is measured at  $T_{ref}=40^\circ$ C. Color code in (a) and (b) is the same.

Comparing dielectric and viscoelastic relaxation data presented in Figure 4 and Figure 5, respectively, reveals a qualitatively good match over the whole frequency range for all blend compositions. In particular, the model captures the speeding up of the long species on dilution with the short species, and also the slowing down of the short species on mixing with the long species. This latter observation is very similar to previous results of Matsumiya et al.<sup>18</sup>

However, a few discrepancies can be observed. The relatively high polydispersity of the long component (PDI=1.08) not taken into account in the simulations, is resulting in a broader experimental  $G''$  peak at low frequency as compared to the simulation data. There are also small discrepancies with the rheological data in the vertical direction, visible (for example) in Figure 3a especially for the two lower molecular weight samples. We consider these discrepancies to be within experimental uncertainty, and that the parameterization is reasonable. We can test this by illustrating the model predictions with the same model parameter  $M_0=1$  kg/mol confronted with LVE data of linear PI measured by Auhl and co-workers.<sup>2</sup> For consistency with the other PI data measured at  $40^\circ$ C we adjust parameter  $G_0$  according to its temperature dependence from 2.85 MPa to 2.71MPa. The comparison presented in Figure 6 shows the quantitative agreement of the model prediction.

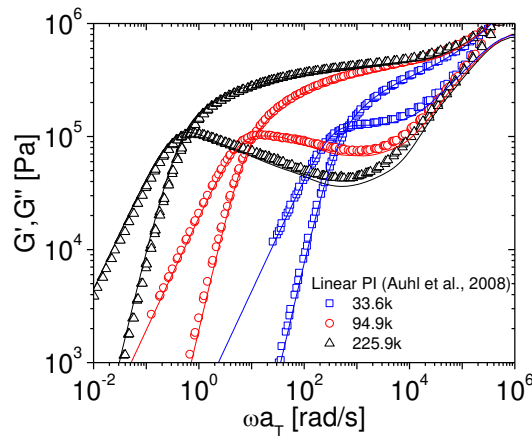


Figure 6: Comparison between simulation results and experimental dynamic complex modulus of monodisperse linear PI with  $M_w=33.6$  kg/mol, 94.9 kg/mol and 225.9 kg/mol. Symbols represent experimental data and lines indicate the SSp predictions. All simulations are obtained with material parameters  $M_0=1$  kg/mol,  $G_0=2.71$  MPa;  $\tau_0=12.1$   $\mu$ s. The experimental data are measured by Auhl and co-workers (Auhl et al., 2008) at  $T_{ref}=25^\circ$ C.

In addition to the small discrepancies in the vertical direction, we also comment on the quality of predictions in the horizontal direction. The model adequately predicts the location of the low frequency peak in the dielectric spectra for all blend compositions. Predictions are excellent for the smaller degrees of dilution, though even at dilutions of 10% and below the agreement in peak position in Figure 4b is within an acceptable factor of 2. The speeding up of terminal relaxation time upon dilution with a faster species is captured. This fact is of some importance for the second part of this study in which we analyze only the longest relaxation times of the end-to-end vector, which approximately correspond to the frequency of this peak.

Simultaneous comparison by two different techniques is a very strong test for the model. Therefore, the overall quality of the SSp model prediction for the viscoelastic and dielectric data can certainly be considered satisfactory.

## **5.2. Comparison with new LVE data: monodisperse, binary and ternary mixtures of linear chains.**

In this section, simulation results of the standard SSp model are compared with our new linear viscoelasticity data. As discussed in the methodology section, we analyze CR of linear probe chains in experimental blends which correspond approximately to the four simplified systems shown in Figure 2, allowing us to separate and analyze the main relaxation contributions. It should be noted that in this section we present PBd data as opposed to the previous section, which presented PI data.

First, we analyze the relatively simple system consisting of a very small fraction of short and/or probe chains diluted in a sea of unrelaxing chains, called “gel chains” (represented by linear PBd chains with  $M_w=305k$ ). Gel chains are effectively immobile in the relaxation timeframe of short and probe chains.

In Figure 7 we compare experimental viscoelastic relaxation data of pure gel chains and their binary mixtures with 20% of short chains ( $M_w=6.9k$ ) or 3% of probe chains ( $M_w=50k$ ). The concentrations are selected in a way that the short or probe chains are only entangled with gel chains. Simulations of all mixtures containing the long gel chains (number of beads equal 804) were made to run for 21 days but the terminal zone for most of the cases was still not reached. However, the covered frequency range is broad enough to include both loss modulus peaks

corresponding to the relaxation of the short and probe chains. The position of these peaks appear to be predicted within factor of 2 in terms of timescale.

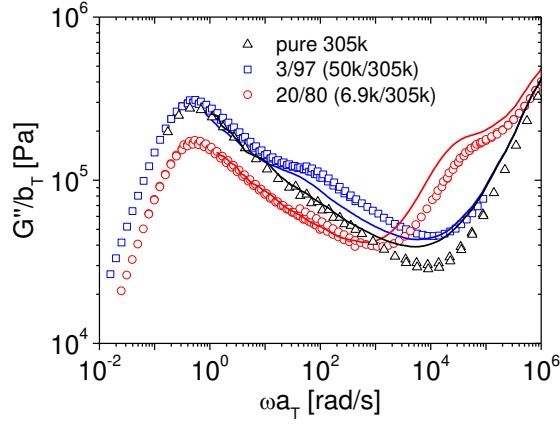


**Figure 7: Linear shear loss modulus of low polydispersity and binary mixtures of Pbd linear chains with  $M_w=6.9k$ ,  $50k$  and  $305k$ . Comparison between simulation predictions (solid lines) and experimental SAOS data (markers). All simulation data obtained using parameters:  $M_0=0.38$  kg/mol,  $G_0=7.0$  MPa and  $\tau_0=0.45$   $\mu$ s. All measurements are conducted at  $T_{ref}=25^\circ\text{C}$ .**

Next, in the system with a small fraction of probe chains diluted in an excess of gel chains, we introduce various fractions of short chains. We expect that short chains will impose CR dynamics on the probe chains and thus we can analyze their effect on relaxation of the end-to-end vector of the probe.

In Figure 8 we present experimental loss modulus data for two ternary mixtures containing 3% probe chains diluted in 20/77 and 80/17 short/gel chains mixtures, respectively.

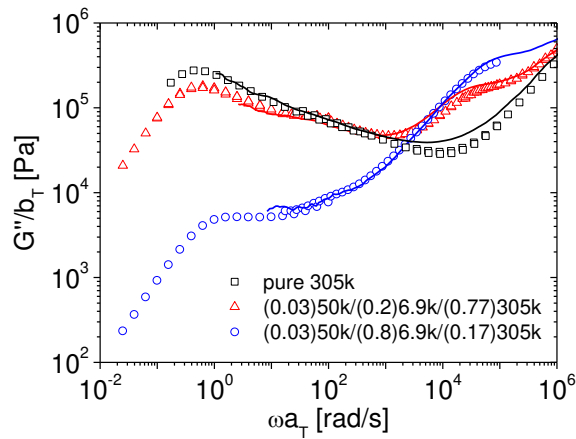


**Figure 8: Linear shear loss modulus of ternary mixtures of Pbd linear chains with 20 and 80wt.% of  $M_w=6.9k$ , 3wt.% of  $50k$ , and 77 and 17wt.% of  $305k$ . The comparison shows simulation predictions (solid**

lines) and experimental SAOS data (markers). All simulation data are obtained using parameters:  $M_0=0.38$  kg/mol;  $G_0=7.0$  MPa and  $\tau_0=0.45$   $\mu$ s. All measurements are conducted at  $T_{ref}=25^\circ$ C.

Finally, we completely substitute gel chains by other probe chains but keeping the same fraction of short chains as in previous systems. By comparison with the previous system, we anticipate to see the effect of other probe chains on the end-to-end vector longest relaxation time.

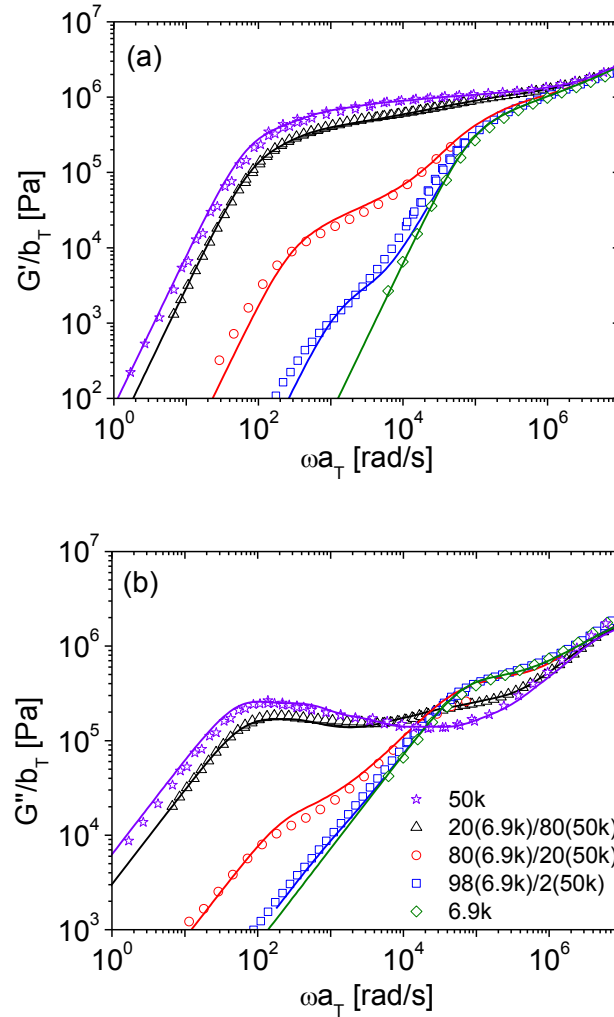


**Figure 9:** Comparison of simulations (solid lines) and experimental SAOS data (markers). Linear shear (a) storage and (b) loss moduli of monodisperse and binary mixtures of PBd linear chains with  $M_w=6.9$ kg/mol and 50kg/mol. All simulation data obtained using parameters:  $M_0=0.38$  kg/mol;  $G_0=7.0$  MPa and  $\tau_0=0.45$   $\mu$ s. Color code in (a) is the same as in (b).

The comparison between linear shear rheology data and simulation results of the SSp model presented in Figures 7 – 9 reveals a satisfactory overlap through the whole covered frequency range for all studied mixtures. However, small discrepancies can be observed. The mismatch in the medium-frequency range for mixtures containing “gel” chains of  $M_w=305$ kg/mol (Figures

7, 8) can be partially attributed to small differences in 1,4-addition content with respect to that of the short and probe chains which were made in a different lab. As noted in section 3.2, these differences led to small irregularities in glass transition temperature, with the glass transition temperature of the “gel” chains being slightly lower than expected for its molecular weight. This may have, to some extent, affected the time-temperature superposition used to create the mastercurves, affecting most strongly the data shifted to higher frequencies (i.e. measured at lower temperatures). Hence, while we can claim satisfactory agreement between the model and data, the remaining discrepancies suggest the need for further experiments, with samples all of identical microstructure made in the same lab. Discrepancies in the high-frequency range can also be attributed to a relatively small average number of beads (4) per slip-link.

Considering the satisfactory simultaneous predictions of viscoelastic and dielectric relaxation data for a set of PI-PI binary blends (section 5.1) and the quantitative prediction of PBd viscoelastic data shown in the present section, we can consider that the SSp model is adequate for analysis of the end-to-end vector relaxation of probe chain affected by CR. We now turn to a detailed analysis of the different relaxation mechanisms present in the SSp model, by comparing tube model predictions with a large set of idealized model simulations.

## **6. Dynamics of probe chains in the SSp model**

In this section, we use the SSp model for simulating dynamics in simplified systems containing probe chains diluted in matrix chains. Here we consider the probe chains to be sufficiently dilute as to be unentangled with other probe chains, but entangled with matrix chains represented by the slip-links. We make a simplifying assumption that these matrix chains give only one, or at most two, constraint release times, so that slip-links are ‘blinking’ at a single or two precise frequencies, which will be varied over a broad range. These idealized systems represent very simplified cases of monodisperse, binary and ternary blends analyzed in section 5 and will be used to improve our theoretical understanding of the CR effect on the relaxation of probe chains.

In the following sections of this study we will derive equations for predicting the longest end-to-end vector relaxation times in the frame of advanced tube theory and confronting them with the SSp simulation data. For the analysis in the frame of tube theory, we utilize a methodology allowing us to calculate the effective friction in the fat tube, recently proposed by Read and co-workers in ref.<sup>22</sup> The central idea of this theory is to separate two independent modes of chain

motion. The first mode is related to longitudinal (i.e. sliding) dynamics of the chain constrained by all types of entanglements. This motion is not affected by the environment, therefore in principle the corresponding friction is just the total chain friction,  $\zeta_0^{cm}=N\zeta_0$ , where  $N$  is the total number of chain beads (Kuhn segments) and  $\zeta_0=1$  is the friction of a single bead (however, as we will discuss below, slip-links make a contribution to this friction).

The second mode is activated by the blinking nature of entanglements and allows the chain to explore new conformations by tube hopping motions in the transverse direction. This second mode depends upon the blinking frequency of entanglements and is further affected by the motion of the chain entrapped inside the tube. Thus for instance for the system #1 shown in Figure 2 this second mechanism is effectively deactivated due to infinitely long CR times of the “gel” chains. In this study, we further investigate a mixing rule proposed in ref.<sup>24</sup> for combining chain friction with friction from CR events.

### 6.1. Relaxation of the probe chain in a single tube without CR.

In this section we analyze the dynamics of probe chains diluted in very long “gel” chains (system#1), where CR is essentially turned off during relaxation of the probe chains. The only active relaxation modes are therefore reptation and contour length fluctuations (CLF) related to longitudinal (i.e. sliding) dynamics of the chain constrained by all entanglements with corresponding friction expected to be the total chain friction,  $\zeta_0^{cm}=N\zeta_0$ , where  $N$  is the total number of chain beads (Kuhn segments) and  $\zeta_0=1$  is the friction of a single bead. Following ref.<sup>15</sup> we therefore expect the terminal reptation time for the chains to be:

$$\tau_d = 3Z\tau_R f(Z) \quad (1)$$

where  $\tau_R=N^2b^2\zeta_0/(3\pi^2k_B T)$  is the Rouse time<sup>7</sup> and  $f(Z) \equiv 1 - \frac{2 \times C_1}{\sqrt{Z}} + \frac{C_2}{Z} + \frac{C_3}{Z^{3/2}}$  represents the correction due to the effect of CLF on chain reptation.<sup>15</sup> However, this expression assumes two things: (i) that we are able to calculate the effective number of entanglements along the “tube” represented by the slip-links, and (ii) that slip-links do not contribute to the effective sliding friction. It turns out that both of these factors are important as we proceed through section 6, in which we attempt to map as closely as possible the correspondence between the SSp model and the tube model. The discussion in Appendix A justifies that the number of entanglements along the tube, defined as  $Z=N/N_e$ , is not equivalent to the average number of slip-springs per chain

in the SSp model. For the “standard” SSp model parameters (see section 4), i.e.  $N_{e,ss}=4$  and,  $N_s=0.5$ , we use equation A1 to estimate that  $N_e=4.89$ . Also, we find that upon reducing the number of slip-links the dilution factor  $\phi$  for the equivalent tube model is almost, but not exactly, the same as the dilution factor  $f$  for number of slip-links in the SSp model. This is because of the finite stiffness of the virtual springs, which allows for extra freedom of the respective entanglement segment as explained in Appendix A. We define this relation between the dilution factors in both models using equation A2 and demonstrate its validity in Figure 10(a).

In addition, we have found that for the implementation of the SSp model used in this paper, with slip-link motion along the chain mediated by Monte Carlo hops between beads, there is a non-negligible contribution to friction for along-tube motion from the slip-links. Appendix B discusses these effects, and the effects of dilution on this friction. The net result is a renormalization of the friction constant per bead for along-tube motion to  $\zeta_{0,tube}$  as given in equation B1.

In Figure 10(a) we present SSp simulation results of linear chains with varying total number of beads,  $N$ , and different average number of beads between two nearest slip-links,  $N_{e,ss}$ . We fit the data using equation B2, with only one parameter,  $\zeta_{0,SL}$ , the effective friction per bead from slip-links in equation B1, which takes a value of 0.55 in the fits shown. Figure 10(a) demonstrates that (i) after normalizing the longest relaxation time by  $3k_{SL}Z\tau_R$ , where  $k_{SL}$  is the factor, defined in Appendix B, by which the along-the-tube motion is slowed down by slip-link friction, the data from a wide range of slip-link dilutions,  $N_{e,ss}=4, 5, 8,$  and  $20$  corresponding to  $f=1, 0.8, 0.5$  and  $0.2$ , can be collapsed essentially to a single curve. This collapse makes use of the dilution factors and adjustments to slip-link friction indicated in equations A2 and B1, respectively. Figure 10(a) also demonstrates that (ii) the simulations are consistent with the Likhtman and McLeish result,<sup>15</sup> equation B2, with the inclusion of slip-link friction. The theoretical predictions shown in Figure A1 by the black solid line correspond to  $f(Z)$  with all prefactors from<sup>15</sup> ( $C_1=1.69, C_2=4.19, C_3=-1.55$ ), which differ only by the last prefactor ( $C_3=-1.4$ ) from fit shown by black dashed line. We introduce this latter correction in order to better fit data points at small  $Z$ . This degree of consistency provides confirmation of our derived value of  $N_e$  and the arguments for the behavior upon dilution.

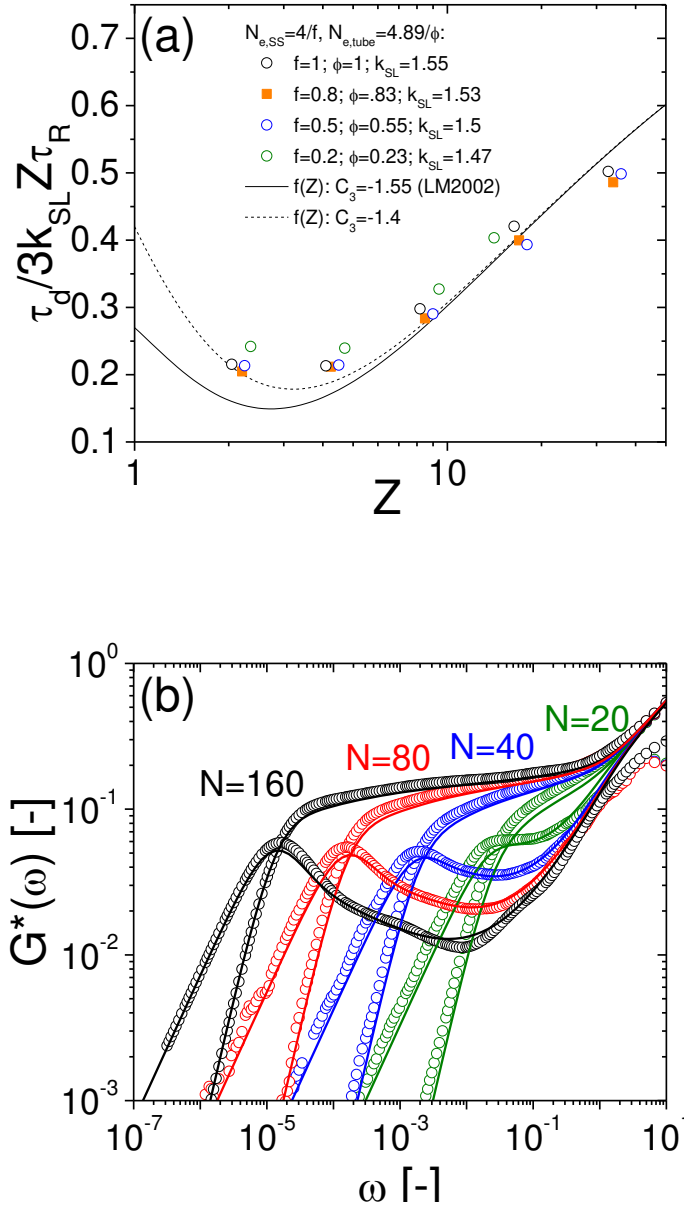


**Figure 10:** (a) Longest relaxation time  $\tau_d$  normalized by pure reptation theory prediction obtained by SSp simulation for linear chains with various number of beads,  $N$ , and different average number of beads between two nearest slip-links,  $N_{e,ss}$  shown by symbols. Black dashed and solid lines show the prediction by the tube model differing by the value of parameter  $C_3=-1.4$  or  $-1.55$ , with the latter used in *Likhtman and McLeish, 2002*; (b) Comparison of dimensionless  $G^*(\omega)$  obtained by the SSp simulations ( $N=20, 40, 80, 160$  and  $N_{e,ss}=4$ ) and fitted using the Likhtman-McLeish tube model ( $N_e=4.89$ ,  $\tau_e=1.25$  and  $G_{N,0}=0.2$ ). The constraint dynamics is deactivated in all simulations and neglected in the tube model predictions.

In all our theoretical predictions using tube theory for fitting SSp simulation data we will always use the parameters  $C_3=-1.4$  and  $N_e=4.89$  obtained in this section.

In Figure 10(b) we show that LVE predictions of the Likhtman-McLeish tube model quantitatively agree with the SSp simulation data over almost the whole frequency range, for a range of chain lengths. These predictions use both plateau modulus and stress equilibration time of a single entanglement strand consistent with  $N_e=4.89$ , i.e.  $G_{N,0}=1/N_e=0.2$  and  $\tau_e=N_e^2 b^2 \zeta_{0,tube}/(3\pi^2 k_B T)=1.25$ , where  $b=1$ ,  $k_B T=1$ ,  $\zeta_{0,tube}=1.55$ . This degree of consistency provides confirmation of our derived value of  $N_e$ . Fits of similar quality can be obtained at other dilutions, by scaling the parameters appropriately.

There is arguably a small discrepancy at high frequencies in Figure 10(b), where Rouse motion within the tube dominates the viscoelastic response. This local Rouse motion is subject to the bead friction of the chain only, whereas the rest of the viscoelastic response from along-the-tube motion and is slowed (by a factor approximately 1.55) by the slip-link friction. Hence, if we apply the Likhtman-McLeish theory to match the whole frequency spectrum and use a single value of  $\tau_e$  which includes the slip-link friction, the high frequency Rouse motion predicted by the theory is marginally slower compared to the simulations. This discrepancy is masked because the simulations do not exhibit a well-developed Rouse spectrum at high frequencies, since there are only a small number of chain beads per slip-link.

## 6.2. Relaxation of the probe chain in a single tube with single CR rate.

We now turn to system#2, which includes, in addition to the reptation sliding motion, constraint release dynamics represented by the “blinking” of the slip-links. In ref. <sup>24</sup> it was shown that in the general case where all entanglements have the same constant CR time, the friction coefficient per bead due to this second mode of motion can be adequately, albeit empirically, represented as follows:

$$\zeta_{TT} = \left( \sqrt{\zeta_{CR,TT}} + \sqrt{\zeta_0^{cm}} \right)^2, \quad (2)$$

where  $\zeta_{CR,TT}$  represents the friction due to the constraint release events and  $\zeta_0$  is the bead friction. The form of equation 2 is a little surprising: one might expect a simple addition of friction factors from the monomers and from the constraint release “hopping” events. In Appendix E we rationalize this crossover formula by considering carefully how the hop length depends upon the constraint release timescale.

The CR friction coefficient  $\zeta_{CR,TT}$  per bead for blinking tube segments in equation 2 and Appendix E is derived from a simple model of particle hopping over a constant distance

$$\zeta_{CR,TT} = \frac{2\tau_{CR}k_B T}{h^2} \frac{1}{N_e}, \quad (3)$$

where  $h$  is an effective hop amplitude per tube segment, the thermal energy  $k_B T=1$ , and  $\tau_{CR}$  is the time between the hops. Although, in the SS<sub>p</sub> model it is actually the moving slip-links which provide the CR motion, we write all theory in this and the following sections in terms of the tube model picture, hence we use the tube parameter  $N_e$ . In the limit of slow constraint release, we anticipate that  $h^2 = \alpha_{CR}^2 N_e b^2$  where  $\alpha_{CR}$  is a yet unknown prefactor. However, as detailed in Appendix E, for fast constraint release, the chain does not have time to reconfigure between CR events, and the effective hop size is smaller. A detailed analysis of this gives rise to a relation of the form of equation 2, whilst retaining linear addition of friction contributions.

By assuming that the two relaxation modes (motion along the tube and CR motion of the tube) are independent we can now compute the longest relaxation time of the chain diluted in the sea of other chains, all having the same molar mass

$$\frac{1}{\tau_p^{(2)}} = \frac{1}{\tau_{TT}} + \frac{1}{\tau_d}, \quad (4)$$

where in case of all entanglements blinking with same frequency  $\tau_{TT}$  represents effective CR Rouse time of the thin tube. This equation represents the competition between reptation and constraint release of the thin tube which is expected as CR rate is varied, as indicated in the Viovy diagram (inset of Figure 2).

As a first guess, we derive  $\tau_{TT}$  by substituting  $\zeta_{TT}$  from equation E5 instead of the bead friction  $\zeta_0$  in the Doi-Edwards equation for Rouse time:  $\tau_R = N^2 b^2 \zeta_0 / (3\pi^2 k_B T)$ .<sup>7</sup>

$$\tau_{TT} = \frac{N^2 b^2}{3\pi^2 k_B T} \zeta_{TT}. \quad (5)$$

However, equation 4 would then involve a small overcounting of relaxation pathways, which becomes apparent in the limit of small (zero) constraint release time  $\tau_{CR}$ . In Appendix F we propose a simple correction applied to  $\zeta_{TT}$  to account for this effect.

For validating the analytical equations derived in this section and Appendices E and F, we run simulations of probe chain dynamics with slip-links blinking at frequency  $1/\tau_{CR}$ , where  $\tau_{CR}$  varies over a broad range of values. This is a simplified model for the probe chains diluted in an excess of ideal monodisperse melt.

For validating the total friction coefficient corresponding to the relaxation of the chain due to constraint release only, we prohibit the chain to release its ends from the slip-links. Thus, reptation is deactivated, but the sliding motion of the slip-links along the rest of the chain allows longitudinal stress equilibration. Apart from that, the only possible relaxation mechanism is the effective CR tube motion. In the following discussion we will refer to the systems where slip-links are not allowed to pass through the chain ends as *non-reptating*, whereas the standard system will be referred to as “*free chain ends*”.

From these simulations we extract the mean square displacement of the center of mass (MSD),  $R_c$ . Assuming that in the *non-reptating* system at  $t \rightarrow \infty$ , tube relaxation is dominated by CR motion, we can thus compute the total thin tube friction coefficient as follows:

$$\zeta^{MSD} = \frac{k_B T}{\lim_{t \rightarrow \infty} \langle R_c^2(t) \rangle / (6t)} \quad (6)$$

Results of these simulations are plotted in Figure 11(a).

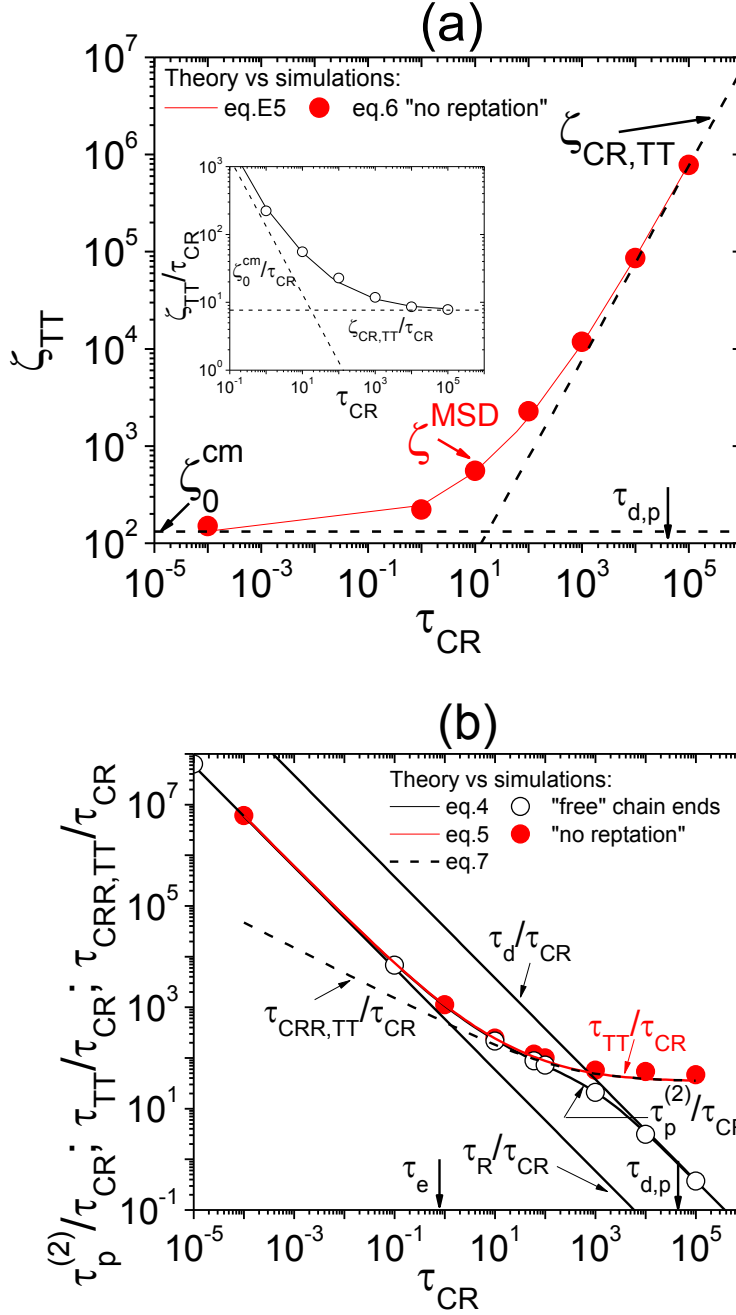


Figure 11: Comparison between theoretical tube predictions (dashed and solid lines) and SSp simulation results (filled and empty circles). All entanglements of the probe chain with number of beads  $N=132$  have the same lifetime,  $\tau_{CR}$ . (a) Effective friction coefficient of the thin tube with probe chain not allowed to reptate. Dashed lines represent  $\zeta_0^{cm}$  and  $\zeta_{CR,TT}$ , corresponding to two extreme cases at  $\tau_{CR} \rightarrow 0$  and  $\tau_{CR} \rightarrow \infty$ , respectively. Filled red circles show obtained by simulations  $\zeta^{MSD}$ . In the inset we show zoomed-in crossover region of  $\zeta_{TT}$  normalized by  $\tau_{CR}$ . The theoretical predictions are made using equation E5 with  $N_e=4.89$ ,  $\alpha_{CR}=1.2$  and  $K=0.36$ . (b) Longest relaxation time of the end-to-end vector of the probe chain in the same systems. Filled red circles and red solid line represent simulation data and theoretical prediction of “non-reptating” chain,  $\tau_{TT}$ . Black empty circles and black solid line represent simulation data and theoretical prediction of the chain with “free” chain ends,  $\tau_p^{(2)}$ . Dashed black line shows longest relaxation time dominated by CR Rouse motion of the thin tube,  $\tau_{CRR,TT}$ . Inclined parallel black thick lines demonstrate longest relaxation times normalized by  $\tau_{CR}$  for relaxation dominated by Rouse motion (on the left) and for reptation of the chain in the thin tube shortened by CLF (on the right). Arrows show stress equilibration

time of a single entanglement strand,  $\tau_e$ , and longest relaxation time of the probe chain in no CR case,  $\tau_{d,p}=36280$ .

By fitting the data on the right-hand side of Figure 11(a) using equation E5 we have extracted the best fit value for parameter  $\alpha_{CR}=1.2$  which defines the jump amplitude of the chain upon disappearance of a single slip-link.

In Figure 11 (b) we plot the longest relaxation times of the end-to-end vector autocorrelation function for the systems with no reptation (red solid line) and chains with free ends (black solid line):  $\Phi(t) = \langle R(t)R(0) \rangle / \langle R_0^2 \rangle$ , where  $R$  is the end-to-end vector of the chain.

The two inclined black solid lines show theoretical values of Rouse and reptation time of the chain normalized by  $\tau_{CR}$ . The exact value of  $\tau_{d,p}=36280$  is obtained from simulating dynamics of the probe chain (of chain length  $N=132$ ) in the no CR case.

The dashed black line in Figure 11(b) represents longest relaxation time dominated by the CR Rouse motion of the thin tube. The tube segment hopping amplitude depends on  $\tau_{CR}$  (see eq. E3) which prevents this line from being horizontal. It is obtained by substituting  $\zeta_{CR,TT}$  (equation 3) into Doi-Edwards equation for Rouse time:<sup>7</sup>

$$\tau_{CRR,TT} = \frac{N^2 b^2}{3\pi^2 k_B T} \zeta_{CR,TT}. \quad (7)$$

Based on Figure 11(b), two dominant scenarios for terminal relaxation can be highlighted depending on the lifetime of the entanglements with respect to relaxation time of the probe chain:

1. Lifetime of entanglements,  $\tau_{CR}$ , is significantly below the Rouse stress equilibration time of a single entanglement strand of the probe chain,  $\tau_e$ . In this case the probe chain is effectively not feeling the presence of the tube and thus completely relaxes by free *Rouse* motion. This is illustrated by the alignment of the data points with the leftmost inclined black solid line.
2. Lifetime of the entanglements is significantly longer than reptation time of the chain, hence the tube is effectively fixed at this time scale and the terminal relaxation is due to chain diffusing along the fixed thin tube.

Between these two regimes, we have a transition zone:

- a. Lifetime of entanglements is longer than entanglement stress equilibration time ( $\tau_{CR} > \tau_e$ ) as indicated by the first inflection point. In this case terminal relaxation is due to CR Rouse tube motion, where the effect of monomer friction on CR hopping amplitude is defined by CR timescale.
- b. In case of ( $\tau_{CR} < \tau_{d,p}$ ) chain reptation contribution becomes important manifesting itself by the second inflection point. The end-to-end vector relaxation terminates by combination of effective CR tube motion and chain reptation in the thin tube. If we now deactivate the chain longitudinal motion the terminal relaxation time will be dominated by CR Rouse tube motion with its hopping amplitude determined by equation E1. Alternatively, by increasing  $\tau_{CR} > \tau_{d,p}$  we effectively deactivate CR and chain relaxes in the same way as in system #1 (Figure 2).

The second transition (b) corresponds to the horizontal line usually drawn on the Viovy diagram (Figure 2, inset) for competition between reptation and constraint release. The first transition (a) would give rise to a second boundary, further up the Viovy diagram, but not necessarily giving a fixed line within the Viovy diagram, which is a two dimensional projection of a larger parameter space.

### **6.3. Two-tube system with a fraction of never relaxing entanglements.**

In order to further increase the complexity with respect to the systems discussed in the previous section, we now consider probe chains constrained by a combination of two types of slip-links: (i) a fraction  $f$  that cannot be deleted due to CR, but only by sliding dynamics of the probe chain, (ii) a remaining fraction  $1-f$  of slip-links blinking at a constant frequency, which is varied over the same range as in the previous section. This is equivalent to the probe chain being entangled with a mixture of gel and short chains, at different compositions. In terms of the tube model, this can be interpreted as a probe chain constrained by both the thin and fat tubes, formed by entanglements with all chains and by entanglements with never relaxing chains, respectively. The thin tube is moving due to CR of short chains, whereas fat tube is fixed. This type of system is shown in Figure 2 (as system #3).

In this system, within the tube picture the chain can be transported along the “fat” tube via two different processes: (i) CR motion of the thin tube, which also involves a contribution from

chain friction as indicated in the previous section, and (ii) motion of the chain along the thin tube contour, which may be projected to give an effective motion along the fat tube. An analysis of this was presented in ref.,<sup>22</sup> building on the earlier work of Viovy.<sup>28</sup> This analysis assumed independence between diffusive transport processes along thin and fat tubes, giving an equation for the friction coefficient per bead of the chain constrained by blinking and permanent entanglements:

$$\frac{1}{\zeta_p^{(3)}} = \frac{1}{\zeta'_{TT}} + \frac{1}{\zeta_{eff}}, \quad (8)$$

where  $\zeta'_{TT} = (1-f)\zeta_{CR,TT} + \zeta_+$ , represents the total friction for hopping of the thin tube consisting of a fraction  $1-f$  of blinking entanglements, and where  $\zeta_+$  represents the contribution of chain friction to the hopping motion. The friction  $\zeta_{eff}$  represents chain motion along the thin tube, but rescaled to give the effective friction for the projected motion along the fat tube.

Equation 8 sets the effective friction constant for all chain motion projected along the fat tube contour. This includes (of course) reptation, but also contour length fluctuations and (if it is considered) the tension re-equilibration process between adjacent fat tube segments.<sup>27</sup> The competition between the two terms in equation 8 gives rise to the line usually drawn on the Viovy diagram (figure 2, inset) representing competition between motion along thin and fat tubes.

For the present SSp simulations, the analysis is made more complicated by the two specific issues identified above in section 6.1 and detailed in Appendices A and B: (i) the fact that the dilution factor  $f$  for the number of slip-links is not the same as the dilution factor  $\phi$  for tube diameter, and (ii) the contribution of slip-links to the sliding friction. We detail the corrections which must be made to the analysis by Read<sup>22</sup> for the SSp simulations in Appendix C. The resulting final expressions for the separate frictions contributions to motion along thin and fat tubes are given in equations C6 to C8 (of Appendix C).

Since both thin tube and chain are relaxing via reptation motion along fat tube contour we can now compute longest relaxation time of the chain as:

$$\tau_p^{(3)} = \frac{L_{FT}^2 N \zeta_p^{(3)}}{\pi^2 k_B T} f(Z^*) = \frac{\phi N^3 b^2 \zeta_p^{(3)}}{N_e \pi^2 k_B T} f(Z^*). \quad (9)$$

In the limit of sufficiently slow constraint release, such that  $\zeta'_{TT} \gg \zeta_{eff}$ , we show in equation C8 (of Appendix C) that  $\zeta_p^{(3)} = (\zeta_0 + \zeta_{0,SL})/\phi$ . In this limit, the factors of  $\phi$  cancel in equation 9, so that it represents reptation purely along the thin tube, including slip-link friction, but written in terms of effective motion along the fat tube coordinates. As constraint release becomes faster, equation 9 includes the faster reptation along the fat tube due to constraint release of the thin tube. In the absence of CLF, this is consistent with the theory of Viovy.<sup>28</sup>

The term  $f(Z^*)$ , determined in equation D4 (of Appendix D), represents correction of the chain reptation time due to CLF motion, where  $Z^*$  is the number of entanglements along the tube in which the dominant CLF motion takes place. Depending on the blend composition and on the constraint release time, this term can represent either CLF in the thin or in the fat tube, or in an effective tube at intermediate length scale. So, the quantity  $Z^*$  could equal  $Z=N/N_e$ , or  $Z_{fat}=N\phi/N_e$ , or some intermediate value. The details on blend compositions and values of  $\tau_{CR,TT}$  associated with different regimes of CLF enhancement are discussed in Appendix D.

For validating these theoretical conclusions, we run simulations of the chain dynamics with a fraction  $1-f$  of slip-links blinking with characteristic time  $\tau_{CR,TT}$  varying over a broad range of values, while others are permanent but can slip along the backbone and thus can only disappear if the probe chain releases its end from the corresponding slip-link by sliding motion.

In Figure 12 for a broad range of  $\tau_{CR,TT}$  values, we plot simulation results of the longest relaxation time of the end-to-end vector of the probe chains. Theoretical predictions plotted as colored lines are computed using equation 9.

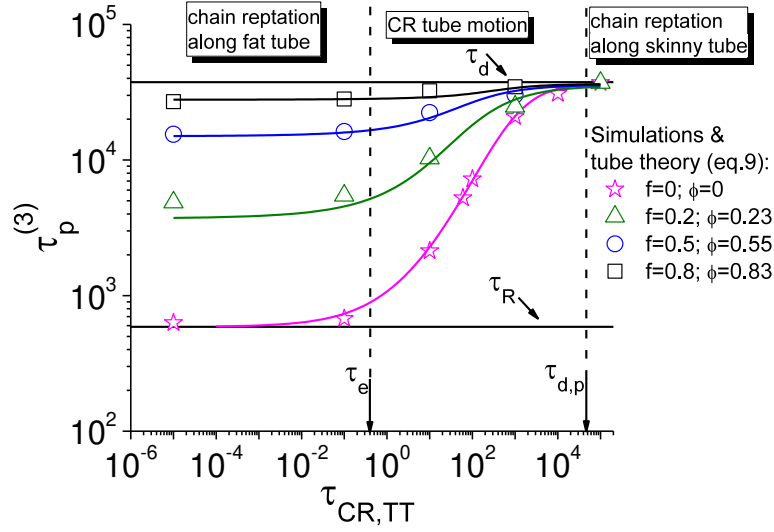


**Figure 12: Comparison between theoretical predictions (color lines) and simulation results (markers) of the end-to-end vector of a probe linear chain with  $N=132$  constrained by blinking and permanent entanglements. Fraction  $1-f$  of blinking entanglements have the same lifetime,  $\tau_{CR,TT}$ . The lowest horizontal black solid line represents terminal relaxation dominated by free Rouse motion of the chain; the uppermost – shortened by CLF reptation of the probe chain. Arrows show stress equilibration time of an entanglement strand,  $\tau_e$ , and longest relaxation time of the probe chain in no CR case,  $\tau_{d,p}=36280$ .**

In Figure 12 the two horizontal black solid lines show theoretical values of  $\tau_R$  and  $\tau_d$  in the thin tube. At intermediate values of  $\tau_{CR,TT}$ , we observe a transition zone with two inflection points reflecting the dominant contribution of CR Rouse tube motion to the terminal relaxation time. After the second inflection point, all curves representing different compositions of blinking and permanent entanglements match the uppermost black solid line representing terminal relaxation dominated by chain diffusing along the fixed thin tube.

With respect to the regimes described in equation D4, most of the presented simulation data, except for  $\phi=0$ , where no effective fat tube exists, are consistent with the first case, where  $Z^*=Z_{fat}$ .

The observed discrepancies at  $\tau_{CR,TT} < \tau_e$  are consistent with those in Figure 10(a), where systems diluted to the effective  $Z < 10$  demonstrate slower longest relaxation time with respect to the theory.

By analyzing the data shown in Figure 12, we can now summarize the results of this section. There are several distinct scenarios for terminal relaxation of this system. However, in practice, the lines between these regimes are not sharp, and all transitions are smooth.

1. At  $\tau_{CR,TT} < \tau_e$ , chain relaxation terminates by chain diffusing in the fat tube with little or no effect from the blinking slip-links;
2. At  $\tau_{CR,TT} > \tau_e$  terminal relaxation is due to effective CR motion of the thin tube controlling both reptation and CLF within a permanent fat tube.
3. At larger values of  $\tau_{CR,TT}$  the second term on the right hand side of equation 8, becomes the dominant contribution, so that chain transport along the thin tube begins to dominate over CR motion of the thin tube. Yet, there remains freedom for CLF along the fat tube contour.
4. At yet slower  $\tau_{CR,TT}$  the thin tube does not even have time to explore locally the fat tube within the CLF timescale, and (according to the regimes noted in equation D4) the system transitions to CLF in the thin tube. At  $\tau_{CR,TT} > \tau_{d,p}$  terminal relaxation is due to chain reptating and performing CLF in the thin tube only.

The third transition corresponds to the line usually drawn on the Viovy diagram for system 3 (figure 2, inset) representing competition between motion along thin and fat tubes. The other transitions would be represented as different boundaries as constraint release rate is varied, but not necessarily giving fixed lines within the Viovy diagram, which is a two dimensional projection of a larger parameter space.

The fourth transition listed above raises an intriguing but speculative possibility. In a monodisperse melt, as terminal relaxation is approached, some constraint release does occur, at a broad range of CR rates coming from fast relaxing chain ends to slower reptation modes. Presumably these CR events lead to a small enhancement of CLF, which can occur in a marginally diluted tube. In contrast, if the same chains are placed in an environment of longer chains, the CR is suppressed, and the CLF will occur only in the narrowest possible tube. Therefore we would anticipate an increase in the terminal relaxation time for short chains placed in a long chain matrix, especially for short chains of only a few entanglements where CLF effects strongly affect the terminal time. This may give a qualitative explanation of the observations of Matsumiya et al.<sup>18</sup> who measured such a retardation, though more work is needed to investigate this. In particular, due to constraints on time and resources, the simulations we present in this paper do not cover the required range of parameters to investigate this point.

In the next section we will further increase complexity of the constraint release environment by permitting motion of previously fixed entanglements. We thereby converge to the case of probe chains relaxing in a binary mixture with two distinct rates of constraint release.

#### 6.4. Systems with two moving tubes.

In this section we discuss the relaxation of probe chains constrained by entanglements with two finite lifetimes. As a representative case of these systems, we analyze probe chains dispersed in a binary blend with shorter chains having fixed CR time and with long chains. The constraint release time of long chains is varied over the broad range of values (see system#4 in Figure 2). Thus, by increasing constraint release time of long chains the system discussed in this section is evolving from the equivalent to system #2 to the system #3 (in Figure 2).

In section 6.3 we have concluded that the total friction of the thin tube constrained by the permanent fat tube,  $\zeta_{TT}'$ , is determined by a combined contributions from  $\zeta_{CR,TT}$  and  $\zeta_+$ .

In order to determine all contributions to the total fat tube friction coefficient,  $\zeta_{FT}$ , we consider two extreme cases with respect to ratio between constraint release rates. In the first scenario lifetimes of the fat tube entanglements are the same as those of the thin tube. In this case we only have a single thin tube and should obtain  $\zeta_{FT}$  equal to  $\zeta_{TT}$  derived in equation E4. On the other hand if lifetime of the “slow” slip-links,  $\tau_{CR,FT}$ , is much larger than those of the fast slip-links,  $\tau_{CR,TT}$ , the total friction coefficient of the fat tube should be dominated by the slower CR motion of the fat tube constraints.

In order to interpolate between these limits, we follow a similar reasoning to the derivation of equation E4. The fraction of slow slip-links per chain is  $f$  and by analogy with equation 3 these provide a friction per chain bead of:

$$\zeta_{CR,FT} = \frac{2\tau_{CR,FT}k_B T}{h_{FT}^2} \frac{f}{N_e}, \quad (10)$$

where  $h_{FT}$  is the typical hop amplitude from the fat tube CR event. In Appendix E we demonstrate how  $h_{FT}$  depends on timescale of the fat tube hopping and on blend composition.

The fraction of fast slip-links is  $1-f$  and so the total friction *per monomer* from both chain friction and thin tube CR events can be estimated using equation E5 as:

$$\zeta_{0,TT} = \frac{2\tau_{CR,TT}k_B T(1-f)}{\alpha_{CR}^2 N_e^2 b^2} \left( 1 + \frac{1}{K} \sqrt{\frac{2\alpha_{CR}^2 N_e^2 b^2 \zeta_0}{k_B T \tau_{CR,TT}}} \right) + \zeta_0. \quad (11)$$

The friction for the fat tube motion can then be found by combining equation 10 (which gives friction from slow CR events), where  $h_{FT}$  is estimated in equation E10 (of Appendix E), and equation 11 (which gives combined friction per monomer from both fast CR events and chain friction). Hence, the total friction per bead due to fat tube motion is:

$$\zeta_{FT} = \zeta_{CR,FT} + \zeta_{0,TT}. \quad (12)$$

For validation of the derived analytical equations, we run simulations of the probe chain entangled with slip-links having two distinct lifetimes  $\tau_{CR,TT}(=60) \gg \tau_e$ , and a wide range of  $\tau_{CR,FT} \geq \tau_{CR,TT}$ . In order to highlight terminal relaxation dominated purely by CR events in the fat tube, we do not allow slip-links to diffuse out of the chain ends thereby prohibiting relaxation by sliding motion of the chain (see Figure 14).

As a first step we verify the scaling of the jumping amplitude of fat tube segments at different polymer concentrations. For this purpose we run simulations of the probe chain ‘‘diluted’’ at different concentrations, having slip-links with lifetime,  $\tau_{CR,FT}$ , varying over a broad range, whereas,  $\tau_{CR,TT}=0$ .

In Figure 13 we demonstrate theoretical predictions of equation 12 compared with friction coefficients obtained from simulating MSD of chain’s center of mass at the limit of  $t \rightarrow \infty$  (see equation 6). The simulations are conducted with good statistics (1000 chains) and long computation time (21 days).

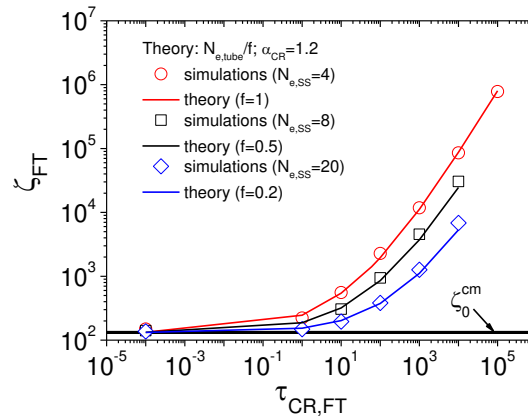


**Figure 13: Total friction coefficient of the fat tube in the binary CR environment. Comparison of the theoretical predictions (solid lines) and the simulation results (markers). In the simulations,  $N_{e,ss}=4, 8$  and**

20 as shown by the red, black and blue symbols, respectively. Lifetime of 1- $f$  fraction of slip-links  $\tau_{CR,TT} = 0$  for all the mixtures. Lifetimes of other slip-links,  $\tau_{CR,FT}$ , vary over a broad range of values.

Comparison between theoretical predictions (equation 12 at the limit of  $\tau_{CR,TT} \rightarrow 0$ ) and simulations in Figure 13 is quantitatively good over the entire range of probed  $\tau_{CR,FT}$ . These results demonstrate that the jumping amplitude of fat tube segments scales as  $\sim N_e \phi^{-0.5}$  similar to the assumption of the tube dilation theory.<sup>9, 17</sup>

Theoretical predictions of the terminal relaxation for freely reptating chains entangled with two types of finite lifetime obstacles can be computed by assuming independence of Rouse motion of the fat tube, with respect to reptation of the thin tube and chain along the fat tube:

$$\frac{1}{\tau_p^{(4)}} = \frac{1}{\tau_{FT}} + \frac{1}{\tau_p^{(3)}}, \quad (13)$$

where longest relaxation time  $\tau_p^{(3)}$  representing the reptative motion of the thin tube and the chain along the fat tube is computed using equation 9 with friction coefficient  $\zeta_p^{(3)}$ , which includes the effects of slip-link friction as shown in equation C8. We note that the above mentioned reptative motion of the thin tube can only be considered when thin and fat tube exist:  $\tau_{CR,TT} > \tau_e$ , and  $\tau_{CR,FT} > \tau_{CR,TT}$  and number of slow entanglements is sufficient to form fat tube.

The longest relaxation time due to CR Rouse motion of the fat tube is computed in analogy with equation 5 as

$$\tau_{FT} = \frac{N^2 b^2}{3\pi^2 k_B T} \zeta_{FT}, \quad (14)$$

where the friction is computed in Equation 12. In appendix F we propose a simple correction of the term  $\zeta_{FT}$  to avoid double counting of the relaxation mechanisms.

In order to validate equations 12 and 14, we run simulations of probe chains constrained by different ratios of slip-links with two distinct lifetimes  $\tau_{CR,TT} = \tau_{d,s} (=60)$  and  $\tau_{CR,FT}$ . As in the simulations presented in Figure 11(a), the slip-links are not allowed to slip through the chain ends and thus chain relaxation is only due to CR motion of the thin and fat tubes.

In Figure 14(a,b) we compare the simulation results and the theoretical predictions. Here, upon increasing  $\tau_{CR,FT}$ , termination by effective thin tube motion combined with Rouse chain motions

at  $\tau_{CR,FT} \sim \tau_{CR,TT}$  is taken over by the effective fat tube motion with a broad transition zone in between.

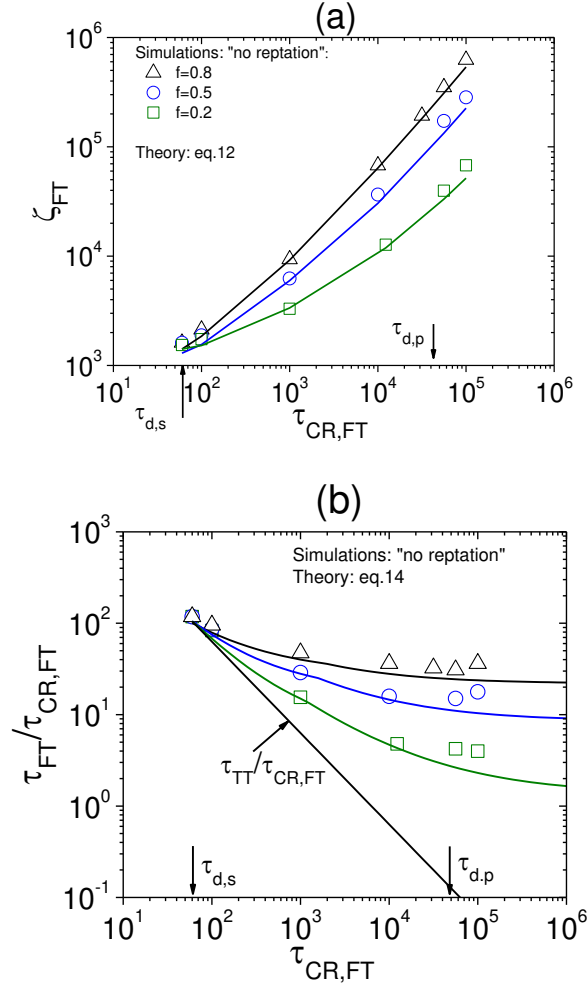


**Figure 14: Comparison of the theoretical predictions (solid lines) and the simulation results (markers). (a) Total friction coefficient of the fat tube in the binary CR environment with  $\tau_{CR,TT}=\tau_{d,s}(=60)$  and various  $\tau_{CR,FT}$ . (b) Longest end-to-end vector relaxation time due to CR motion of the fat tube (equation 14), normalized by  $\tau_{CR,FT}$ . Inclined black solid line corresponds to extreme case when all entanglements have the same lifetime  $\tau_{CR,TT}$ . Arrows show longest relaxation time of the short,  $\tau_{CR,TT}=\tau_{d,s}$  ( $=60$ ), and probe chains,  $\tau_{d,p}=36280$ , in no CR case. The fractions of the slow slip-links,  $f=0.2$ ,  $0.5$  and  $0.8$  as indicated by black, blue and green symbols, respectively. Color code in (a) and (b) is the same.**

In order to validate equation 13 we run simulations of the probe chains constrained by different ratios of slip-links with two distinct lifetimes  $\tau_{CR,TT}$  and  $\tau_{CR,FT}$ . In these simulations the slip-links can freely diffuse out of the chain ends thus permitting chain relaxation by reptation and CLF. In Figure 15 we compare simulation results of this model with the theoretical predictions of equation 13.

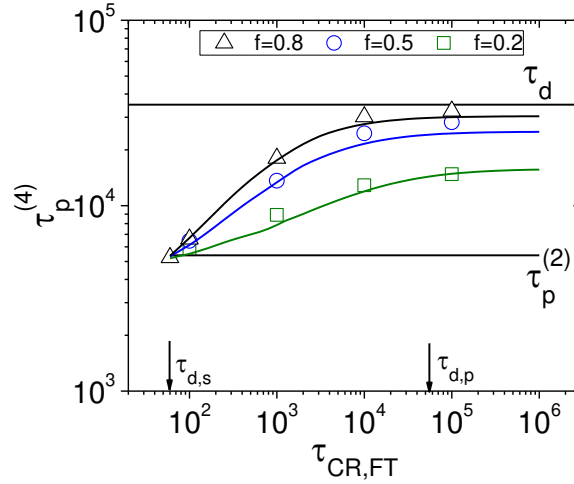


**Figure 15: Longest relaxation time of the end-to-end vector of the probe chain with free chain ends in binary CR environment of different compositions. The theoretical predictions (equation 13) shown by solid color lines are superimposed with the simulation data (markers). In all mixtures lifetime of entanglements with short chains  $\tau_{CR,TT}=60$ , whereas all entanglements with long chains have lifetime,  $\tau_{CR,FT} \geq \tau_{CR,TT}$ . The lowermost horizontal black solid line corresponds to extreme case when all entanglements have the same lifetime and relax by the effective thin tube motion,  $\tau_p^{(2)}$ ; the uppermost – affected by CLF reptation of the probe chain in the fixed thin tube. Arrows show longest relaxation times of the short chains,  $\tau_{CR,TT}=\tau_{d,s}=60$ , and probe chain in no CR case,  $\tau_{d,p}=36280$ .**

In Figure 15, all possible longest relaxation times depending on characteristic times and fractions of the fast and slow entanglements are localized between two horizontal black solid lines designating theoretically predicted terminal relaxation due to CR motion of the thin tube, and chain reptation along the thin tube shortened by CLF, respectively.

Unlike the systems discussed in sections 6.2 and 6.3 the data points show a very broad shoulder spanning the range  $\tau_{CR,TT} < \tau_{CR,FT} < \tau_{d,p}$ . This can be explained by a more complex correlation between all involved relaxation mechanisms, that significantly blurs separation of a single dominant relaxation mechanism from the analyzed combinations of  $\tau_{CR,TT}$ ,  $\tau_{CR,FT}$  and  $\tau_{d,p}$ .

Comparison between the simulations and the theory can be characterized as quantitatively good at all probed  $\tau_{CR,FT}$ . However, the quality of prediction varies depending on composition of the CR environment. The observed slight discrepancies at the right-hand side in Figure 15 are consistent with those observed in the transition zone in Figure 12, which, in turn, are consistent with slight discrepancies in Figure 10(a).

To summarize, in this system with probe chains constrained by two types of entanglements, appearing and disappearing at constant frequencies  $1/\tau_{CR,TT} = 1/60$  and  $1/\tau_{CR,FT} \leq 1/\tau_{CR,TT}$ , the terminal relaxation of the chain can be determined by one of the following scenarios:

- (1) If  $\tau_{CR,FT} \sim \tau_{CR,TT}$  then relaxation terminates by effective CR motion of the single thin tube. In this case depending on the ratio between  $\tau_{CR}$  and  $\tau_{d,p}$  terminal relaxation can also be dominated by chain reptation along the thin tube;
- (2) If  $Z_{fat} \gg 1$  and  $\tau_{CR,TT} < \tau_{CR,FT} < \tau_{d,p}$  the relaxation terminates by combination of the effective CR motion of the fat and thin tubes;
- (3) If  $\tau_{CR,FT} > \tau_{d,p}$  the relaxation terminates by the correlated reptative motion of the chain along the thin tube and CR motion of thin tube along the fat tube. This scenario is equivalent to the transition zone in Figure 12, described by scenario 2 at the end of previous section.

## 7. Conclusions

In this paper we have solved a set of simple problems for understanding the effect of CR on the relaxation dynamics of entangled chains. We have proposed and verified a method for predicting the effect of several CR environments on the relaxation of the end-to-end vector of probe chains in well controlled “model systems” containing slow chains and/or fast relaxing chains. Experimental data have been confronted with simulations by the SSp model, which was later used as a benchmark for validating predictions by a detailed tube model. For the latter, we have followed the CR picture reported by Viovy *et al.*<sup>28</sup> and implemented and refined the effective fat tube friction and the CLF contribution in the analyzed CR environments based on ideas of Read *et al.*<sup>22</sup> The main results are as follows:

- The SSp model is capable to simultaneously predict the viscoelastic and dielectric relaxations of monodisperse and binary melts of linear polymers using the same set of parameters consistent with those used in previous works. It is thus a valid benchmark for testing higher level (in the sense of coarser description) tube theories.
- The proposed theoretical framework, based on refined tube theory, quantitatively captures results of SSp simulations of chain dynamics in various CR environments. This good agreement between tube theory and the SSp model predictions gives some hope that these seemingly different approaches can be reconciled and unified. Specifically, in Appendix G, we summarize some key results in terms of the tube model parameters to aid comparison with the experiments.

- Our theoretical predictions in line with experimental observations of Matsumiya and co-workers<sup>18</sup> demonstrate that CR does contribute to dielectric relaxation of linear probe chains. We have also shown that the longest relaxation time of the end-to-end vector of the probe chain is in fact affected by dynamics of all topological constraints with a lifetime shorter than the chain's own bare reptation time shortened by CLF.

Finally, the SSp model can serve as a versatile research tool, “*an idealized numerical experiment*”, providing detailed information on individual relaxation mechanisms which can be turned on and off at will, and suitable for further developing current understanding of multi-chain effects in tube models, applied to systems with complex constraint release environments, i.e. polydisperse in chain length and even architecture. The methodology developed in this work can be easily extended to include a larger number of constraint release rates.

#### **Appendix A: Mapping dilution effects in tube and SSp models.**

In the limit of point-like slip-springs (in which the restraining spring is infinitely stiff) we might expect the number of beads per entanglement in the tube model representation to be  $N_e = N_{e,ss}$  (the average number of beads between slip-springs). However, since the restraining springs in SSp model have a finite spring constant, the slip-links explore a finite volume and this effectively smooths the mean path of the tube, so that chain beads need to travel a shorter curvilinear distance to relax by reptation. It also reduces the plateau modulus, because the chains are less constrained overall. Both of these effects can be interpreted as an increase in the effective number of beads per (tube) entanglement,  $N_e$ . The analysis leading to Eq 28 of ref.<sup>23</sup>, for springs uniformly distributed along the chain, indicates the effective enhancement factor with respect to the modulus is  $\sqrt{1+4n_s}$ , where  $n_s = N_s / N_{e,ss}$  is the ratio of number of beads in the virtual spring to the beads between slip-springs. In what follows, we shall take this to be the correct enhancement factor in the present SSp simulations, i.e.

$$N_e = N_{e,ss} \sqrt{1+4n_s} \quad (\text{A1})$$

The number of entanglements along the tube is defined as  $Z=N/N_e$ . For the “standard” SSp model parameters (see section 4), using  $N_{e,ss}=4$  and,  $N_s=0.5$ , this gives  $N_e=4.89$ .

One corollary to this discussion, particularly relevant to the blend calculations, concerns the effect of dilution of slip-springs on the effective tube dilution. As the number of constraining slip-springs decreases, they become more “point-like” with respect to the length scale of the tube diameter. If the slip-springs are diluted by a factor  $f$ , so that  $N_{e,ss}(f)=N_{e,ss}/f$ , then we can define a tube dilution factor,  $\phi$ , such that  $N_e(f)=N_e/\phi$ . In general it is not true for the SSp model that  $\phi = f$  exactly. Instead, using the previous equation, we find:

$$\phi = N_e(1)/N_e(f) = f \frac{\sqrt{1+4n_s}}{\sqrt{1+4fn_s}}, \quad (\text{A2})$$

where we assume  $N_s$ , representing stiffness of virtual springs, to remain constant at different concentrations.

In our simulations of experimental systems, constraint release is always modeled by a pairwise connection between slip-links. This may be expected to give an effective dilution exponent of  $d=1$  in the equivalent tube theory. This dilution, however, applies to the slip-link dilution factor  $f$ . Hence, the tube diameter dilution of the variable  $\phi$  implied by equation A2 is very marginally weaker than implied by an exponent of  $d=1$ , though it approaches exponent of  $d=1$  for small  $\phi$ , when the slip-links become equivalent to point-like slip-links.

### **Appendix B : Slip-link friction.**

When comparing the predictions of equation 1 to our data for the terminal relaxation time of chains within the SSp model, we found evidence that the slip-springs themselves provide a non-negligible contribution to the effective friction for along-the-tube motions, i.e. to both reptation and CLF. This effect could be reduced by increasing the number of Monte Carlo hopping attempts per time step. In all results presented in section 6 we use 10 attempts per slip-spring, per time step (this accelerates the terminal relaxation, but increasing further had no significant effect). We believe, however, that there remains a slip-link contribution to the friction which is intrinsic to the simulations, most likely arising from the use of Monte Carlo hops between beads in the limit where the stiffness for the virtual springs is significantly greater than the stiffness of the spring between beads. In this limit, slip-link hops to adjacent beads are relatively unlikely events in the Monte Carlo scheme, because adjacent beads are usually further away than the

typical fluctuation volume of a virtual spring. As a result, a successful, permanent hop to an adjacent bead typically needs to wait for a favorable local rearrangement of the chain, bringing adjacent beads into the locality of the slip-spring. Hence the “hopping time” for the beads is slaved to the chain motion, and this gives rise to larger than anticipated slip-link friction.

In this Appendix we present a simple analysis of the slip-link friction, obtaining the (perhaps surprising) result that the slip-link friction per chain-bead, for along-the-tube motion, is almost independent of dilution. The anticipated reduction in friction from fewer slip-springs is compensated, almost exactly, by the increased number of hops between monomers required to allow motion along the fatter tube. As a result, the effective friction per bead for along-the-tube motion in a diluted tube can be written as:

$$\zeta_{0,tube} = \frac{f}{\phi} \zeta_{0,SL} + \zeta_0 \quad (\text{B1})$$

where  $\zeta_{0,SL}$  is a constant governing the effective friction per bead from slip-links, in the undiluted tube and  $\zeta_0$  is the monomeric friction. We then replace equation 1 with:

$$\tau_d = 3k_{SL}Z\tau_R f(Z) \quad (\text{B2})$$

where  $k_{SL} = \zeta_{0,tube} / \zeta_0$  is the factor by which the along-the-tube motion is slowed down by slip-link friction.

Below we derive a simple expression for slip-link friction contributions to along-the-tube motion and its behavior in dilution. We suppose a slip-link makes a “successful” and uncorrelated hop to an adjacent bead on average every time  $\Delta t_{SL}$ . We note that  $\Delta t_{SL}$  may be expected to be significantly larger than the hopping attempt time, since in the SSp model the virtual spring stiffness is larger than the bead-bead spring stiffness. Thus, typically adjacent beads are further away than the typical fluctuation volume of a slip-link, and even if a hop is occasionally “allowed” to a high energy state on an adjacent bead, it will quickly be followed by a correlated hop back. Thus, successful, uncorrelated hops require significant local rearrangement of the chain.

Hops to adjacent beads allow the slip-link to diffuse back and forth along the chain. In time  $t$ , the mean square number of beads from its initial position will therefore be:

$$n^2 = \frac{t}{\Delta t_{SL}} \quad (\text{B3})$$

So, the time required to hop  $N_e$  monomers (equivalent to motion of one diameter along the tube) is:

$$t = N_e^2 \Delta t_{SL} \quad (\text{B4})$$

Hence, the effective diffusion constant along the tube contour is

$$D = \frac{a^2}{2t} = \frac{N_e b^2}{2N_e^2 \Delta t_{SL}} = \frac{b^2}{2N_e \Delta t_{SL}}. \quad (\text{B5})$$

This corresponds to a friction constant, *per slip-link*, of

$$\frac{k_B T}{D} = N_e \frac{2k_B T \Delta t_{SL}}{b^2}. \quad (\text{B6})$$

Since there are  $N_{e,ss}$  beads per slip-spring, the friction constant per bead is therefore:

$$\zeta_{0,SL} = \frac{N_e}{N_{e,ss}} \frac{2k_B T \Delta t_{SL}}{b^2}. \quad (\text{B7})$$

Upon dilution of slip-links,  $N_{e,ss}$  is increased by a factor  $1/f$ , whilst  $N_e$  increases by a different factor  $1/\phi$ , as detailed in Appendix A.  $f$  and  $\phi$  are almost, but not exactly, the same, so consequently the effective friction per chain bead from slip-links is almost unchanged by dilution, giving the factor  $f \cdot \zeta_{0,SL} / \phi$  in equation B1.

### Appendix C: Friction for “fat tube” motion in SSp model.

We first reproduce the derivation of the effective friction coefficient for fat tube motion proposed by Read and co-workers.<sup>22</sup>

In the limit of small  $\tau_{CR,TT}$  ( $\zeta_{CR,TT} \rightarrow 0$ ) the chain friction per bead must always remain  $\zeta_0$  regardless of  $f$ . This condition is satisfied by introducing the additional chain friction contribution,  $\zeta_+$ :

$$\lim_{\tau_{CR,TT} \rightarrow 0} \frac{1}{(1-f)\zeta_{CR,TT} + \zeta_+} + \frac{1}{\zeta_{eff}} = \frac{1}{\zeta_0} \quad (C1)$$

In this equation  $\zeta_{CR,TT}$  is defined for the fraction of blinking entanglements  $1-f$  using equation 3.  $\zeta_{eff}$  is the effective friction coefficient due to the sliding motion of the chain projected on the fat tube contour,  $L_{FT}=\phi^{1/2}L$ . The theoretical expression for this projected motion can be derived by recognizing that, in a system where reptation is the only relaxation mechanism, the escape times of the chain from the thin tube and the fat tube are the same. Therefore, in the absence of slip-link friction:

$$\zeta_{eff} L_{FT}^2 = \zeta_0 L^2.$$

Thus, the effective friction per bead for the chain's sliding motion projected on the fat tube contour can be computed as:

$$\zeta_{eff} = \frac{\zeta_0}{\phi}. \quad (C2)$$

Next, by substituting equation C2 in equation C1 we can derive an expression for the additional chain friction contribution per bead which ensures that at the limit of very fast CR events total chain frictions remains equal to  $\zeta_0$ :

$$\zeta_+ = \frac{\zeta_0}{1-\phi}. \quad (C3)$$

It is possible to follow the same line of reasoning with the addition of slip-link friction and careful consideration of dilution effects. We first note, from equation B1, that we expect the effective friction for motion along the (diluted) fat tube to take the form:

$$\zeta_p^{(3)} = \frac{f}{\phi} \zeta_{0,SL} + \zeta_{fat} \quad (C4)$$

in which the first term  $f \cdot \zeta_{0,SL} / \phi$  represents the friction from the fraction  $f$  of slip-springs with “slow” constraint release which define the fat tube. Any motion along the “fat tube” must involve chain motion through these slip-springs, and so they contribute directly to the friction. The extra friction  $\zeta_{fat}$  represents all other friction contributions. In the limit when constraint release from the “fast” slip-springs is extremely fast i.e.  $\tau_{CR,TT} \rightarrow 0$  then these slip-springs contribute no friction, and the only friction comes from the chain, i.e.  $\zeta_{fat} = \zeta_0$ . In all other cases,

we need to combine friction contributions from chain motion, constraint release and slip-link friction in an appropriate way.

Following presented above arguments, we assume independence of transport processes for motion of the chain along the thin tube and constraint release of the thin tube along the fat tube.

Hence

$$\frac{1}{\zeta_{fat}} = \frac{1}{\zeta_{TT}'} + \frac{1}{\zeta_{eff}} \quad (C5)$$

where  $\zeta_{TT}' = (1-f)\zeta_{CR,TT} + \zeta_+$  represents the total friction for hopping of the thin tube constrained by a fraction  $1-f$  of blinking entanglements, and where  $\zeta_+$  represents the contribution of chain friction to the hopping motion. The friction  $\zeta_{eff}$  represents chain motion along the thin tube, but rescaled to give the effective friction for the projected motion along the fat tube in an analogous manner to the derivation of equation C2. The simple crossover formula employed in eq.C5 provides a smooth transition between two regimes. The physics captured by this formula is identical to that described eq.17 in Viovy et al.,<sup>28</sup> in section 3 in Read et al.<sup>22</sup> and eq.19 in van Ruymbeke et al.<sup>26</sup> However, the latter one makes use of a more sharp transition between different regimes implemented through a “max” function.

However, we must also include the contribution of slip-link friction to this motion, from a fraction  $1-f$  of slip-links, and so:

$$\zeta_{eff} = \frac{\zeta_0 + (1-f)\zeta_{0,SL}}{\phi} \quad (C6)$$

where the slip-link friction  $\zeta_{0,SL}$  does not carry the extra factor  $f/\phi$  because we are examining motion along the undiluted tube. Finally, insisting that  $\zeta_{fat} = \zeta_0$  in the limit  $\tau_{CR,TT} \rightarrow 0$  allows us to obtain:

$$\zeta_+ = \frac{\zeta_0(\zeta_0 + (1-f)\zeta_{0,SL})}{(1-\phi)\zeta_0 + (1-f)\zeta_{0,SL}}. \quad (C7)$$

These equations guarantee two important limits. When constraint release is fast, we obtain equation B1 as the friction for motion along the fat tube. Conversely, in the limit of slow constraint release such that  $\zeta_{TT}' \gg \zeta_{eff}$ , we note that  $\zeta_{fat} \approx \zeta_{eff}$  and so:

$$\begin{aligned}\zeta_p^{(3)} &= \frac{f}{\phi} \zeta_{0,SL} + \frac{\zeta_0 + (1-f)\zeta_{0,SL}}{\phi} \\ &= \frac{\zeta_0 + \zeta_{0,SL}}{\phi}\end{aligned}\tag{C8}$$

This gives the friction for motion along the (undiluted) thin tube, including slip-link friction, but rescaled to give the effective friction along the fat tube.

#### Appendix D: Determination of the effective tube for contour length fluctuations.

In this appendix we demonstrate how the effective tube diameter in which CLF motion takes place is determined by the blend composition and CR timescale.

We first consider the timescale for CLF along the fat tube. Recognizing that  $\zeta_p^{(3)}$  obtained in equation 8 is the effective friction constant for chain motion projected onto the fat tube coordinate, the timescale for CLF in the fat tube is obtained as the Rouse time calculated using  $\zeta_p^{(3)}$  as the chain friction. This gives:

$$\tau_{CLF, fat} = \frac{N^2 b^2}{3\pi^2 k_B T} \zeta_p^{(3)}.\tag{D1}$$

In the limit of slow constraint release such that  $\zeta_p^{(3)} = (\zeta_0 + \zeta_{0,SL})/\phi$ , we find  $\tau_{CLF, fat} = k_{SL} \tau_R / \phi$  where  $k_{SL} = (\zeta_0 + \zeta_{0,SL})/\zeta_0$  is the factor by which the along-tube motion is slowed down by SSp friction. This is exactly in line with the enhanced stretch relaxation time identified by Auhl et al., (2009). Since both reptation and CLF along the fat tube are governed by the same friction factor  $\zeta_p^{(3)}$ , the whole dynamics is consistent with projection of the chain motion along the fat tube, i.e. taking  $Z^* = Z_{fat}$  with CLF in the fat tube.

This conclusion remains valid unless constraint release of the thin tube is so slow that the thin tube does not have chance to explore, locally, the fat tube within this CLF timescale. If this is the case then there is not sufficient freedom for CLF to occur fully in the fat tube. The timescale for local equilibration of these monomers is the CR Rouse time of their subsection of thin tube, i.e.

$$\tau_{e,fat} = \tau_{TT} \left( \frac{N_e}{N\phi} \right)^2, \quad (D2)$$

where  $\tau_{TT}$  is as given in equation 5. If  $\tau_{e,fat} < \tau_{CLF,fat}$  then we expect CLF in the fat tube, i.e.  $Z^* = Z_{fat}$ . This condition usually only breaks down in the limit of slow constraint release such that  $\tau_{CLF,fat} = k_{SL}\tau_R / \phi$  and where  $\zeta_{TT} \approx \zeta_{CR,TT}$  in equation 2 so that:

$$\tau_{e,fat} = \frac{2\tau_{CR,TT}}{3\pi^2\alpha_{CR}^2\phi^2}. \quad (D3)$$

In this case, the condition  $\tau_{e,fat} < \tau_{CLF,fat}$  becomes a condition on the constraint release timescale:

$$Z^* = Z_{fat} \text{ if } \tau_{CR,TT} < \frac{3\pi^2\alpha_{CR}^2}{2} k_{SL}\phi\tau_R.$$

The other limiting case occurs where constraint release is so slow that  $\tau_{CR,TT} \gg \tau_R$  so that no significant constraint release occurs during the timescale  $\tau_R$  for CLF in the thin tube. Then, CLF occurs dominantly in the thin tube and  $Z^* = Z$ .

Intermediate between these two limiting cases is a regime in which contour length fluctuations occur whilst the thin tube simultaneously undergoes constraint release Rouse motion. In this case, CLF effectively occurs in an intermediate ‘‘supertube’’ defined by dilution factor  $\phi^*$ , which we obtain by equating  $\tau_{e,fat} = \tau_{CLF,fat}$  with the replacement  $\phi = \phi^*$ . In this intermediate regime,  $Z^* = N\phi^* / N_e$ . Putting all three regimes together:

$$\begin{aligned} Z^* &= Z_{fat} & \tau_{CR,TT} &< \frac{3\pi^2\alpha_{CR}^2 k_{SL}}{2} \phi\tau_R \\ Z^* &= \phi^* Z = \frac{2}{3\pi^2\alpha_{CR}^2 k_{SL}} \frac{\tau_{CR,TT}}{\tau_R} Z & \frac{3\pi^2\alpha_{CR}^2 k_{SL}}{2} \phi\tau_R &< \tau_{CR,TT} < \frac{3\pi^2\alpha_{CR}^2 k_{SL}}{2} \tau_R \quad (D4) \\ Z^* &= Z & \tau_{CR,TT} &> \frac{3\pi^2\alpha_{CR}^2 k_{SL}}{2} \tau_R \end{aligned}$$

For validating these theoretical conclusions, we run simulations of the chain dynamics with a fraction  $1-f$  of slip-links blinking with characteristic time  $\tau_{CR,TT}$  varying over a broad range of values, while others are permanent but can slip along the backbone and thus can only disappear if the probe chain releases its end from the corresponding slip-link by sliding motion.

In Figure D1 for a broad range of  $\tau_{CR,TT}$  values, we plot simulation results of the longest relaxation time of the end-to-end vector of the probe chains. Theoretical predictions plotted as solid color lines are computed using equation 9.

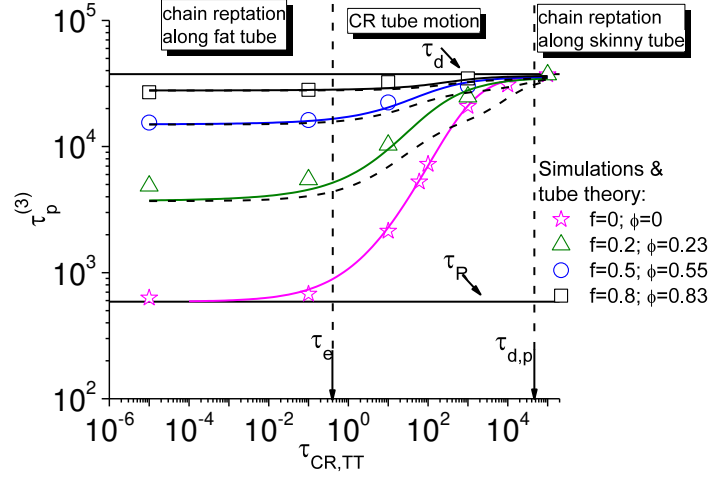


**Figure D1:** Comparison between theoretical predictions (lines) and simulation results (markers) of the end-to-end vector of a probe linear chain with  $N=132$  constrained by blinking and permanent entanglements. The lines show prediction of equation 9 with different CLF regimes described in equation D4. The crossover between different regimes is fitted using eq. D5 with parameter  $\beta=0.25$  (color solid lines) and  $\beta=1$  (dashed black lines). Fraction  $1-f$  of blinking entanglements have the same lifetime,  $\tau_{CR,TT}$ . The lowest horizontal black solid line represents terminal relaxation dominated by free Rouse motion of the chain; the uppermost – shortened by CLF reptation of the probe chain. Arrows show Rouse entanglement relaxation time  $\tau_e = \tau_R/Z^2$  and longest relaxation time of the probe chain,  $\tau_{d,p}=36280$ .

To implement a continuous transition between various regimes derived in equation D4 we use a simple crossover formula which in the limit of  $\tau_{CR} \gg \tau^*$  converges to  $f(Z^*)=f(Z)$  but when  $\tau_{CR} \ll \tau^*$  leads to  $f(Z^*)=f(Z_{fat})$  and at intermediate values we get  $f(Z^*)=f(Z, \phi^*)$ :

$$f(Z^*) = f(A.Z), \quad (D5)$$

where

$$\frac{1}{A} = 1 + \frac{1}{\left( \left( \frac{\tau_{CR,TT}}{\tau^*} \right)^\beta + \left( \phi(1-\phi)^{-1} \right)^\beta \right)^{1/\beta}} \quad (D6)$$

with the characteristic time

$$\tau^* = \frac{3\pi^2 \alpha_{CR}^2 k_{SL} \tau_R}{2}. \quad (D7)$$

The theoretical predictions demonstrated in Figure D1 by color solid lines are obtained with  $\beta=0.25$ . We also plot predictions with  $\beta=1$  (black dashed lines) to demonstrate the effect of fitting parameter  $\beta$ .

We note that the crossover formula D6 is purely empirical and is solely used to capture the onset of tube dilation from constraint release Rouse motion in an SSp model, and then arrest of tube dilation as the fat tube diameter is approached. The exact physics of this transition is not clear to us and this is one of the reasons why we demonstrate predictions with different parameter  $\beta$  in Figure D1.

## Appendix E: Tube hop amplitude due to CR event.

*Thin tube.*

The analysis presented here below rationalizes the empirical mixing law (equation 2), which was used by Shivokhin et al.<sup>24</sup>

When the constraint release time is long, the hop length,  $h$ , is expected to be proportional to the typical tube diameter, hence:

$$h^2 = \alpha_{CR}^2 N_e b^2, \quad (\text{E1})$$

where  $b=1$  is the size of the Kuhn segment, and  $\alpha_{CR}$  is a yet unknown prefactor. A previous publication,<sup>24</sup> did not include the natural scaling with  $N_e$  in either equation 3 or E1, and so used a different variable  $A_{CR}$ , related to  $\alpha_{CR}$  as  $A_{CR}=\alpha_{CR}N_e$ . We determine value of  $\alpha_{CR}(=1.2)$  by fitting simulation data in Figure 11(a).

Significantly, equation 2 is obtained under the assumption that equation E1 gives the hop size independently of the constraint release timescale. However, if the constraint release timescale is short, such that the local Rouse motion of the chain does not permit a significant change in local chain configuration between CR events, then the expected hop length must be smaller, limited by how far a monomer on the chain can move during the constraint release timescale. This can be estimated by equating the constraint release timescale with the Rouse time of a subsection of chain containing  $n_{CR}$  monomers, giving:

$$n_{CR} = \sqrt{\frac{3\pi^2 k_B T \tau_{CR}}{b^2 \zeta_0}}. \quad (\text{E2})$$

The hop length is then expected to be of order  $h^2 \approx cn_{CR}b^2$  where  $c$  is an, as yet unknown, constant. In order to interpolate the hop length between the limits of short and long constraint release time, we might use a simple crossover formula:

$$h^2 = b^2 \left( \frac{1}{cn_{CR}} + \frac{1}{\alpha_{CR}^2 N_e} \right)^{-1}. \quad (\text{E3})$$

Now, using equations 3, E2 and E3 together, and adding in the direct contribution of monomer friction, we find the friction per bead for the second mode of chain motion, through constraint release hops:

$$\begin{aligned} \zeta_{TT} &= \zeta_{CR,TT} + \zeta_0 \\ &= \frac{2\tau_{CR}k_B T}{b^2} \frac{1}{N_e} \left( \frac{1}{\alpha_{CR}^2 N_e} + \frac{1}{c} \sqrt{\frac{b^2 \zeta_0}{3\pi^2 k_B T \tau_{CR}}} \right) + \zeta_0. \end{aligned} \quad (\text{E4})$$

Because of the square root dependence of  $n_{CR}$  in equation E2, the form of this equation E4 is remarkably similar to that of equation 2. In fact, for the very specific choice

$$c^2 = \frac{\alpha_{CR}^2}{6\pi^2}$$

equation E4 becomes *exactly* identical to equation 2 (where in equation 2, we use equation E1 for the hop size). It may be noted that the monomer friction contributes at two levels in equation E4. Firstly there is the direct contribution from  $\zeta_0$ . Secondly, the monomer friction can limit the scale of the hopping during CR events. It is this second contribution which gives rise to the type of crossover function captured in equation 2, rationalized in equation E4. More generally, we can treat  $c$  as a fitting parameter, which we parameterize as:

$$c^2 = K \frac{\alpha_{CR}^2}{6\pi^2}$$

so that equation E4 becomes:

$$\begin{aligned} \zeta_{TT} &= \zeta_{CR,TT} + \zeta_0 \\ &= \frac{2\tau_{CR}k_B T}{\alpha_{CR}^2 N_e b^2} \left( 1 + \frac{1}{K} \sqrt{\frac{2\alpha_{CR}^2 N_e^2 b^2 \zeta_0}{k_B T \tau_{CR}}} \right) + \zeta_0. \end{aligned} \quad (\text{E5})$$

We find the best fit in the crossover region of  $\zeta_{TT}$  (in the inset of Figure 11(a) by introducing prefactor  $K(=0.36)$ .

*Fat tube.*

In the limit of extremely slow constraint release, such that the chain, and the thin tube have a great deal of time for local rearrangement between fat tube CR events, we anticipate the typical hop amplitude should follow the dilation of the fat tube diameter, i.e.

$$h_{FT}^2 = \frac{\alpha_{CR}^2 N_e b^2}{\phi}. \quad (\text{E6})$$

However, if the fat tube constraint release timescale is shorter, then the effective hop length may be smaller, being limited by both chain friction and the friction from CR hops of the thin tube. These prevent the chain and thin tube from moving a large distance during a slow CR event.

The hop length for slow CR events can be estimated by equating the slow CR time  $\tau_{CR,FT}$  with the Rouse time (including total friction as given by equation 11) of a subsection of chain containing  $n_{CR,FT}$  monomers, so that:

$$n_{CR,FT} = \sqrt{\frac{3\pi^2 k_B T \tau_{CR,FT}}{b^2 \zeta_{0,TT}}}. \quad (\text{E7})$$

The hop length is then expected to be of order  $h_{FT}^2 \approx cn_{CR,FT} b^2$ . In order to interpolate between this and the limit of equation E6, we use a crossover formula:

$$h_{FT(1)}^2 = b^2 \left( \frac{1}{cn_{CR,FT}} + \frac{\phi}{\alpha_{CR}^2 N_e} \right)^{-1}. \quad (\text{E8})$$

If timescale of the slow constraint release is allowed to approach that of the fast constraint release, then it is expected that the hopping length for ‘‘slow’’ CR events must be the same as that for ‘‘fast’’ CR events, i.e. it would approach the equivalent of equation E3:

$$h_{FT(2)}^2 = b^2 \left( \frac{1}{c} \sqrt{\frac{b^2 \zeta_0}{3\pi^2 k_B T \tau_{CR,FT}}} + \frac{1}{\alpha_{CR}^2 N_e} \right)^{-1}. \quad (\text{E9})$$

In fact, setting  $\tau_{CR,FT} = \tau_{CR,TT}$  in equation E8 always underpredicts  $h^2$  compared to equation E9, but the discrepancy is within a of 2. This indicates that equation E8 captures the correct physics, but with just a small discrepancy due to the fact that equations 11 and E7 assume that a

continuous chain Rouse model is appropriate. This assumption breaks down as  $\tau_{CR,FT}$  approaches  $\tau_{CR,TT}$  since only a few fast CR hops occur for each slow CR event. A very simple interpolation formula, provides the correct scaling for large  $\tau_{CR,FT}$  and guarantees the correct result when  $\tau_{CR,FT}=\tau_{CR,TT}$  :

$$h_{FT}^2 = \max(h_{FT(1)}^2, h_{FT(2)}^2). \quad (\text{E10})$$

## Appendix F.

In this appendix we propose a simple method to eliminate overcounting of relaxation pathways which can ultimately cause overprediction of the longest relaxation times.

*Thin tube:*

A small overcounting of relaxation pathways becomes apparent in the limit of small (zero) constraint release time  $\tau_{CR}$  in equation 4. In this limit, we require that the relaxation time  $\tau_p^{(2)}$  from equation 4 should equal the Rouse time  $\tau_R$ , but there is a danger that the combination of Rouse relaxation and reptation implied by equation 4 predicts a faster terminal time. Hence, we use:

$$\tau_{TT} = \frac{N^2 b^2}{3\pi^2 k_B T} \tilde{\zeta}_{TT}, \quad (\text{F1})$$

where the monomer friction in  $\tilde{\zeta}_{TT}$  is marginally modified from equation E5:

$$\tilde{\zeta}_{TT} = \frac{2\tau_{CR} k_B T}{\alpha_{CR}^2 N_e^2 b^2} \left( 1 + \frac{1}{K} \sqrt{\frac{2\alpha_{CR}^2 N_e^2 b^2 \zeta_0}{k_B T \tau_{CR}}} \right) + \zeta_0 \left( 1 - \frac{1}{3k_{SL} Z f(Z)} \right)^{-1}. \quad (\text{F2})$$

The extra factor  $\left( 1 - \frac{1}{3k_{SL} Z f(Z)} \right)^{-1}$  in this equation removes the overcounting of relaxation pathways and ensures that equation 4 reduces to the Rouse time,  $\tau_R$ , when constraint release is fast. This correction factor is in some ways equivalent to the  $(1 - \phi)^{-1}$  correction factor present for  $\zeta_+$  in equation C3, as derived in ref. <sup>22</sup>

*Fat tube:*

The longest relaxation time due to CR Rouse motion of the fat tube is computed as

$$\tau_{FT} = \frac{N^2 b^2}{3\pi^2 k_B T} \tilde{\zeta}_{FT}, \quad (\text{F3})$$

where the friction is computed in a manner similar to Equation 12, but with a correction to avoid, at an approximate level, the overcounting in Equation 13 of relaxation pathways between motion along the fat tube, and constraint release motion:

$$\tilde{\zeta}_{FT} = \zeta_{CR,FT} + \tilde{\zeta}_{0,TT} \left( 1 - \frac{1}{3k_{SL}Z_{fat}f(Z^*)} \right)^{-1}. \quad (\text{F4})$$

The correction factor  $\left( 1 - \frac{1}{3k_{SL}Z_{fat}f(Z^*)} \right)^{-1}$  is similar to the factor from equation F2, but now applied at the level of the fat tube.

Since there are fewer fat tube segments than thin tube segments, the correction in equation F4 is more substantial than that applied in equation F2. There are evidently problems with this approach for small volume fractions when the factor  $3k_{SL}Z_{fat}f(Z^*)$  approaches unity, but in this limit the number of entanglements along the fat tube is less than one, and it ceases to be appropriate to consider the existence of a fat tube at all.

### **Appendix G. Recast of key results in “tube model parameters”.**

Most of the results presented in section 6, and in the Appendices, relate to comparison between the tube model and the SSp model, and so all results are presented in simulation units. There are also several specific complications arising from the SSp model itself, namely the issues of slip-link friction, and effects of dilution, which might not be relevant in real polymer systems (though there is certainly the possibility of equivalents, such as extra friction from entanglements). One reviewer of this paper made a (very reasonable) request that some of the rather complicated results be presented in “tube model parameters” to aid comparison with experiments. We show this in two specific cases.

The “system #2” case, dealt with in section 6.2, corresponds to a dilute long chain in a matrix of short chains, and it may be anticipated that the terminal relaxation crosses from reptation and

contour length fluctuations, for long “short chains” and large values of  $\tau_{CR}$ , towards terminal relaxation via constraint release Rouse motion. In our theory, this crossover is handled by equation 4 giving the terminal time  $\tau_p^{(2)}$ :

$$\frac{1}{\tau_p^{(2)}} = \frac{1}{\tau_{TT}} + \frac{1}{\tau_d}. \quad (\text{G1})$$

This crossover function was sufficient for our simulated systems, in which the long chains have rather few entanglements. More complicated crossover functions may be needed for the general case of longer chains. In entanglement units, the reptation time for the long chains with number of entanglements  $Z_L$  is given by equation 1:

$$\tau_d = 3Z_L \tau_e f(Z_L) = 3Z_L^3 \tau_e f(Z_L) \quad (\text{G2})$$

The constraint release Rouse time  $\tau_{TT}$  depends on the values of  $\tau_{CR}$ , which depends on the length of the short chain. In a real blend, there is in fact a spectrum of constraint release times, so we can only make an approximation. Let us suppose that the terminal reptation time of the short chains determined the constraint release time, and parameterize this as:

$$\tau_{CR} = \frac{3\pi^2 \alpha_{CR}^2 \beta}{2} \tau_{d,s}, \quad (\text{G3})$$

where  $\beta$  is a parameter to be determined and  $\tau_{d,s}$  is the terminal time of the short chains, with  $Z_s$  entanglements, given by:

$$\tau_{d,s} = 3Z_s^3 \tau_e f(Z_s). \quad (\text{G4})$$

Substituting from G3 into equations 5 and F2, and then rearranging gives:

$$\tau_{TT} = Z_L^2 \left[ \beta \tau_{d,s} \left( 1 + \frac{2}{K} \sqrt{\frac{\tau_e}{\beta \tau_{d,s}}} \right) + \tau_e \left( 1 - \frac{1}{3Z_L f(Z_L)} \right)^{-1} \right]. \quad (\text{G5})$$

The later terms in this expression handle the case where there is a crossover for very small  $\tau_{d,s}$  towards unentangled chain Rouse motion. For larger  $\tau_{d,s}$  we simply get the standard constraint release Rouse result,  $\tau_{TT} = \beta\tau_{d,s}Z_L^2$ .

The results of section 6.3 for “system #3” may be considered to be relevant to long chains entangled with other long chains (giving a fat tube) and with short chains (giving the thin tube). The main result for the terminal time, equation 9, may be written as:

$$\tau_p^{(3)} = 3\phi Z_L^3 \tau_e f(Z_L^*) \frac{\zeta_p^{(3)}}{\zeta_0}, \quad (\text{G6})$$

where the function  $f(Z_L^*)$  switches between CLF in fat and thin tubes (see equation D4) and the friction constant ratio determines whether chain motion along the thin tube or fat tube is fastest, and is given by:

$$\frac{\zeta_0}{\zeta_p^{(3)}} = \frac{1}{(1-\phi) \frac{\zeta_{CR,TT}}{\zeta_0} + (1-\phi)^{-1}} + \phi \quad (\text{G7})$$

and

$$\frac{\zeta_{CR,TT}}{\zeta_0} = \frac{\beta\tau_{d,s}}{\tau_e} \left( 1 + \frac{2}{K} \sqrt{\frac{\tau_e}{\beta\tau_{d,s}}} \right). \quad (\text{G8})$$

The first term in equation G7 gives diffusion along the fat tube, mediated by constraint release, whilst the second term gives motion along the thin tube.

## Acknowledgements

We thank Dietmar Auhl and Hiroshi Watanabe for kindly supplying experimental data of “monodisperse” and binary mixtures of linear Polyisoprene. We also acknowledge fruitful discussions with Jorge Ramirez, Jing Cao and Zuwei Wang on the subject of SSp friction. We are grateful to the reviewers for their valuable comments, which helped us to significantly improve clarity and overall quality of the manuscript. The research leading to these results has

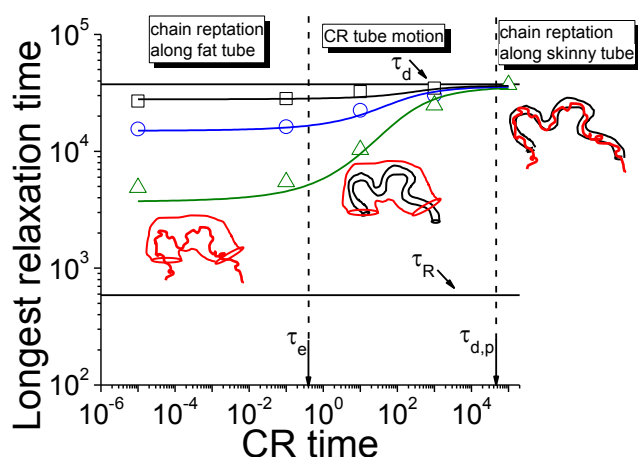
received funding from the [European Community's] Seventh Framework Programme [FP7/2007-2013] under Grant Agreement No. 214627-DYNACOP and A.E.L. acknowledges the support of EPSRC grant EP/K017683. Computational resources have been provided by the supercomputing facilities of the Université catholique de Louvain (CISM/UCL) and by the Center for Molecular Study of Condensed Soft Matter ( $\mu$ CoSM/IIT).

## References:

1. Auhl, D.; Chambon, P.; McLeish, T. C. B.; Read, D. J. Elongational Flow of Blends of Long and Short Polymers: Effective Stretch Relaxation Time *Phys. Rev. Lett.* **2009**, 103,136001.
2. Auhl, D.; Ramirez, J.; Likhtman, A.E.; Chambon, P.; Fernyhough, C. Linear and non-linear shear flow behavior of monodisperse Polyisoprene melts with a large range of molecular weights *J. Rheol.* **2008**, 52, 801.
3. Daoud, M.; de Gennes, P.-G. Some remarks on the dynamics of polymer melts. *J. Polym. Sci., Polym. Phys. Ed.* **1979**, 17, 1971.
4. de Gennes, P.G. Collapse of a polymer chain in poor solvents. *J.Phys.Lett. (Paris)* **1975**, 36, 55.
5. de Gennes, P.G. Reptation of a Polymer Chain in the Presence of Fixed Obstacles *J. Chem. Phys.* **1971**, 55, 572.
6. Desai, S.P.; Kang, B.-G.; Katarova, M.; Hall, R.; Huang, Q.; Lee, S.; Shivokhin, M.; Chang, T.; Venerus, D.C.; Mays, J.; Schieber, J.D.; Larson, R.G. Challenging Tube and Slip-Link Models: Predicting the Linear Rheology of Blends of Well-Characterized Star and Linear 1,4-Polybutadienes. *Macromolecules* **2016**, 49, 4964.
7. Doi, M.; Edwards, S. F. *The Theory of Polymer Dynamics*; Oxford University Press: New York, **1986**.
8. Doi, M.; Edwards, S.F.. Dynamics of concentrated polymer systems. Part 1.— Brownian motion in the equilibrium state. *J.Chem.Soc., Faraday Trans. 2* **1978**, 74, 1789
9. Doi, M.; Graessley, W.W.; Helfand, E.; Pearson, D.S. Dynamics of polymers in polydisperse melts. *Macromolecules* **1987**, 20, 1900
10. Ferry, J.D. *Viscoelastic properties of polymers*. John Wiley & Sons, New York, 1980.
11. Glomann, T.; Schneider, G.J.; Bras, A.; Pyckhout-Hintzen, W.; Wischniewski, A.; Zorn, R.; Allgaier, J.; Richter, D. Unified Description of the Viscoelastic and Dielectric Global Chain Motion in Terms of the Tube Theory. *Macromolecules* **2011**, 44(18), 7430
12. Klein, J. The Onset of Entangled Behavior in Semidilute and Concentrated Polymer Solutions. *Macromolecules* **1978**, 11, 852.
13. Likhtman, A. E. Single-Chain Slip-Link Model of Entangled Polymers: Simultaneous Description of Neutron Spin-Echo, Rheology, and Diffusion. *Macromolecules* **2005**, 38, 14.

14. Likhtman, A. E. Viscoelasticity and molecular Rheology. In: A comprehensive Reference; Elsevier B.V.: Amsterdam, **2012**; pp 133–179.
15. Likhtman, A. E.; McLeish, T. C. B. Quantitative Theory for Linear Dynamics of Linear Entangled Polymers. *Macromolecules* **2002**, 35, 6332.
16. Liu, C.-Y.; Halasa, A.F.; Keunings, R.; Bailly, C. Probe rheology: A simple method to test tube motion. *Macromolecules* **2006**, 39, 7415
17. Marucci, G. Relaxation by Reptation and Tube Enlargement: A Model for Polydisperse Polymers. *J. Polymer science* **1985**, 23, 159.
18. Matsumiya, Y.; Kumazawa, K.; Nagao, M.; Urakawa, O.; Watanabe, H. Dielectric Relaxation of Monodisperse Linear Polyisoprene: Contribution of Constraint Release. *Macromolecules* **2013**, 46(15), 6067
19. Pilyugina, K.; Andreev, M.; Schieber, J.D. Dielectric Relaxation as an Independent Examination of Relaxation Mechanisms in Entangled Polymers Using the Discrete Slip-Link Model. *Macromolecules* **2012**, 45(14), 5728
20. Ramirez, J.; Likhtman, A.E. RepTate software: <http://reptate.com>, **2009**.
21. Ramirez, J.; Sukumaran, S. K.; Likhtman, A. E. Significance of cross correlations in the stress relaxation of polymer melts *J. Chem. Phys.* **2007**, 126 (24), 244904.
22. Read, D. J.; Jagannathan, K.; Sukumaran, S. K.; Auhl, D. A full-chain constitutive model for bidisperse blends of linear polymers *J. Rheol.* **2012**, 56, 823.
23. Read, D.J.; Jagannathan, K.; Likhtman, A.E. Entangled Polymers: Constraint Release, Mean Paths, and Tube Bending Energy. *Macromolecules* **2008**, 41, 6843-6853
24. Shivokhin, M.E.; van Ruymbeke, E.; Bailly, C.; D. Kouloumasis, N.; Hadjichristidis, N.; Likhtman, A.E. Understanding Constraint Release in Star/Linear Polymer Blends. *Macromolecules* **2014**, 47(7), 2451
25. Stockmayer, W.H. Dielectric dispersion in solutions of flexible polymers. *Pure Appl. Chem.* **1967**, 15, 539
26. van Ruymbeke, E.; Shchetnikava, V.; Matsumiya, Y.; Watanabe, H. Dynamic Dilution Effect in Binary Blends of Linear Polymers with Well-Separated Molecular Weights. *Macromolecules* **2014**, 47, 7653
27. van Ruymbeke, E.; Masubuchi, Y.; Watanabe, H. Effective Value of the Dynamic Dilution Exponent in Bidisperse Linear Polymers: From 1 to 4/3. *Macromolecules* **2012**, 45, 2085
28. Viovy, J. L.; Rubinstein, M.; Colby, R. H. Constraint release in polymer melts: tube reorganization versus tube dilation. *Macromolecules* **1991**, 24, 3587.
29. Watanabe, H. Investigation of Entanglement Dynamics of Flexible Polymer Chains via Comparison of Dielectric and Viscoelastic Properties: A Review of Recent Findings. *Kor.-Austr. Rheol. J.* **2001**, 13, 205.
30. Watanabe, H.; Ishida, S.; Matsumiya, Y.; Inoue, T. Viscoelastic and Dielectric Behavior of Entangled Blends of Linear Polyisoprenes Having Widely Separated Molecular Weights: Test of Tube Dilation Picture. *Macromolecules* **2004**, 37, 1937; **2004**, 37, 6619.

For table of contents use only:



## UNDERSTANDING THE EFFECT OF CONSTRAINT RELEASE ENVIRONMENT ON THE END-TO-END VECTOR RELAXATION TIME OF LINEAR CHAINS.

Maksim E. Shivokhin<sup>1,2,3\*</sup>, Daniel J. Read<sup>4\*</sup>, Dimitris Kouloumasis<sup>5</sup>, Rok Kocen<sup>1</sup>, Flanco Zhuge<sup>1</sup>,  
Christian Bailly<sup>1</sup>, Nikos Hadjichristidis<sup>6</sup>, Alexei E. Likhtman<sup>7</sup>

<sup>1</sup>Bio- and Soft Matter division (BSMA), Institute of Condensed Matter and Nanosciences (IMCN), Université Catholique de Louvain (UCL), Place Croix de Sud 1, 1348 Louvain-la-Neuve, Belgium

<sup>2</sup>Center for molecular study of condensed soft matter and Department of Chemical and Biological Engineering, Illinois Institute of Technology, 3440 South Dearborn Street, Chicago, Illinois 60616, USA

<sup>3</sup>Current affiliation: ExxonMobil Chemical Company, Baytown Technology and Engineering Complex, 5200 Bayway Drive, Baytown, Texas 77520, USA

<sup>4</sup>School of Mathematics, University of Leeds, Leeds LS2 9JT, U.K

<sup>5</sup>Laboratory of Industrial Chemistry, Department of Chemistry, University of Athens, Panepistimiopolis Zografou, 157 71 Athens, Greece

<sup>6</sup>Physical Sciences and Engineering Division, KAUST Catalysis Center (KCC), Polymer Synthesis Laboratory, King Abdullah University of Science and Technology (KAUST), Thuwal 23955-6900, Kingdom of Saudi Arabia

<sup>7</sup>School of Mathematical and Physical Sciences, University of Reading, Reading RG6 6AX, U.K.